Modelling post-plasma quenching nozzles for improving the performance of CO_2 microwave plasmas

Modelling post-plasma quenching nozzles for improving the performance of CO_2 microwave plasmas

Senne Van Alphen[1,2], Ante Hecimovic[4], Christian K. Kiefer[4], Ursel Fantz[4], Rony Snyders[2,3], Annemie Bogaerts[1]

[1] Research group PLASMANT, University of Antwerp, Belgium

[2]Research group ChIPS, University of Mons, Belgium

[3]Materia Nova Research Center, Avenue Copernic 3, Parc Initialis, 7000 Mons, Belgium

[4] Max-Planck-Institut für Plasmaphysik, Germany

Abstract

Given the ecological problems associated to the CO_2 emissions of fossil fuels, plasma technology has gained interest for conversion of CO_2 into value-added products. Microwave plasmas operating at atmospheric pressure have proven to be especially interesting, due to the high gas temperatures inside the reactor (i.e. up to 6000 K) allowing for efficient thermal dissociation of CO_2 into CO and O_2. However, the performance of these high temperature plasmas is limited by recombination of CO back into CO_2 once the gas cools down in the afterglow. In this work, we computationally investigated several quenching nozzles, developed and experimentally tested by Hecimovic et al.,[1] for their ability to quickly cool the gas after the plasma, thereby quenching the CO recombination reactions. Using a 3D computational fluid dynamics model and a quasi-1D chemical kinetics model, we reveal that a reactor without nozzle lacks gas mixing between hot gas in the center and cold gas near the reactor walls. Especially at low flow rates, where there is an inherent lack of convective cooling due to the low gas flow velocity, the temperature in the afterglow remains high (between 2000 and 3000 K) for a relatively long time (in the 0.1 s range). As shown by our quasi-1D chemical kinetics model, this results in a important loss of CO due to recombination reactions. Attaching a nozzle in the effluent of the reactor induces fast gas quenching right after the plasma. Indeed, it introduces (i) more convective cooling by forcing cool gas near the walls to mix with hot gas in the center of the reactor, as well as (ii) more conductive cooling through the water-cooled walls of the nozzle. Our model shows that gas quenching and the suppression of recombination reactions have more impact at low flow rates, where recombination is the most limiting factor in the conversion process.

1. Introduction

Mitigation of global warming, caused by enhanced greenhouse gas concentrations in the Earth's atmosphere, is considered one of the main challenges of the 21st century.[2] The International Energy Association (IEA) has calculated that, in order to have a 50% chance of restricting global warming to 2°C, CO_2 emissions must be reduced by 17 Gt in 2030 and by 39 Gt in 2050 against projected emissions.[3] In this context, plasma technology is gaining increasing interest for carbon capture and utilization (CCU), i.e. capturing CO_2 that would otherwise be emitted into the atmosphere and converting it into value-added chemicals and renewable fuels, thereby closing the so-called "carbon loop".[4,5] Plasmas are electricity-driven, which fits perfectly within the future energy landscape that is expected to move towards renewable electricity sources (solar, wind, etc.).[6] Plasma conversion technology has several advantages with respect to other emerging electro- and photochemical technologies: (i) the technology is inherently flexible, and therefore suitable for intermittent renewable energy supplies, (ii) it is a relatively low cost technology as plasma reactors don't rely on critical raw materials, (iii) plasma chemistry is not limited to occur on the surface of an electrode (like in electro- and

photocatalysis) as it takes place virtually in the entire plasma volume, and (iv) the technology is easily scalable due to its simple design.[7]

Plasma-based CO_2 conversion has been studied in various types of plasma reactors[4,6], but microwave (MW) plasmas have proven to be especially interesting for CO_2 dissociation, being electrode-free, thus avoiding electrode degradation over time, and achieving very high conversion and energy efficiency.[8–11] MW plasmas display different characteristics depending on the operating pressure. At low pressures, i.e. below 100 mbar, the plasma is radially expanded to almost fill up the whole quartz tube, operating in the so-called diffuse mode.[12] At higher pressure, the plasma is confined in a narrow filament in the center of the reactor, operating in the contracted mode.[12] Recent studies strongly suggest that the CO_2 dissociation process in both modes heavily relies on the thermal dissociation pathway.[13] Especially in the contracted mode, where the discharge is confined in a small volume, thermal dissociation is the dominant pathway. The small plasma volume results in a high power density and a high local specific energy input (SEI), yielding gas temperatures up to 6000 K.[10,12] While at these high temperatures CO_2 is fully dissociated, only conversions around 10% at energy efficiencies around 30% are measured at pressures close to 1 atm.[9,10] This is attributed to the recombination of CO back into CO_2, once the gas slowly cools down after leaving the plasma:

$$CO + O + M \rightleftarrows CO_2 + M$$

$$CO + O_2 \rightleftarrows CO_2 + O$$

It has been suggested that fast cooling of the gas after the plasma can quench the recombination reactions, effectively "freezing" the conversion that was achieved in the hot plasma.[9] Modelling work by Vermeiren and Bogaerts showed that for warm plasmas with high specific energy input (SEI ≥ 2 eV/molecule) quenching at the point of maximum conversion inside the plasma could enhance the conversion and energy efficiency by up to a factor 3.[14] Next to limiting the recombination reactions, and thus freezing the formed reaction products (so-called ideal quenching), it is also possible to even further dissociate CO_2 upon quenching. This is called super-ideal quenching and was predicted by Vermeiren and Bogaerts to occur at low SEI (ca. 0.5 eV/molecule) when a vibrational nonequilibrium, created or enhanced by the sudden drop in gas temperature, promotes further dissociation of CO_2:[14]

$$CO_2(v) + O \rightleftarrows CO + O_2$$

in which $CO_2(v)$ represents a vibrationally excited CO_2 molecule.

Recently, the beneficial effect of quenching was experimentally shown by Hecimovic et al.[1] by using nozzles of varying diameter in the effluent of a MW plasma torch. The aim of the nozzle was to force mixing of the hot plasma gas with the surrounding colder gas to induce cooling and reduce the recombination reactions. Significant improvements of the conversion and energy efficiency were observed, especially at higher pressures (900 mbar) and low CO_2 flow rates (< 10 slm), which, at a plasma power of 1500 W, corresponds to an SEI above 2 eV/molecule. At 5 slm, 1500 W and 900 mbar, the conversion in a reactor without nozzle was measured to be about 5%, while attaching a 2.5 mm nozzle enhanced the conversion to 35%, which is a 7-fold increase.

Given the exceptional performance of the nozzle configuration demonstrated by Hecimovic et al., we aim in this paper to reveal in detail the gas flow behavior and quenching mechanism of the nozzle by means of computational modelling. Through computational fluid dynamics (CFD), we will simulate the gas flow and heat transfer within the reactor that was operated by Hecimovic et al. and how this is influenced by attaching a nozzle in the effluent. Subsequently, we will use a quasi-1D chemical kinetics model to reveal the effect of the nozzle on the underlying chemistry. The most significant results of Hecimovic et al. were found at the highest investigated pressure, i.e. 900 mbar. This pressure was used

for the measurements, but experiments performed at 900 mbar and at atmospheric pressure yield identical CO_2 conversion,[15] thus results presented at 900 mbar are representative for atmospheric pressure operating conditions as well. As atmospheric pressure regimes are also most interesting for practical (industrial) applications, we will focus on this pressure regime in the present study as well, but to be consistent with the experiments, the CFD model is also performed at 900 mbar.

2. Methodology

2.1 Calculating the gas flow and heat transfer in a 3D fluid dynamics model

To reveal the effect of a nozzle in the effluent of the MW plasma reactor, we developed a three-dimensional (3D) CFD model that calculates the flow behavior and heat transfer within the gas flowing through the plasma torch in COMSOL Multiphysics.[16] The 3D model geometry of the MW reactor, as described by Hecimovic et al., is shown in figure 1. The finite element mesh of the simulation domain is shown in the Supplementary Information (SI, section S.1). Note that we have to use a 3D model, due to the swirl flow established by the four tangential gas inlets. Although a 2D model would be faster, it would require specific approximations about this swirl flow which do not fully reflect reality.

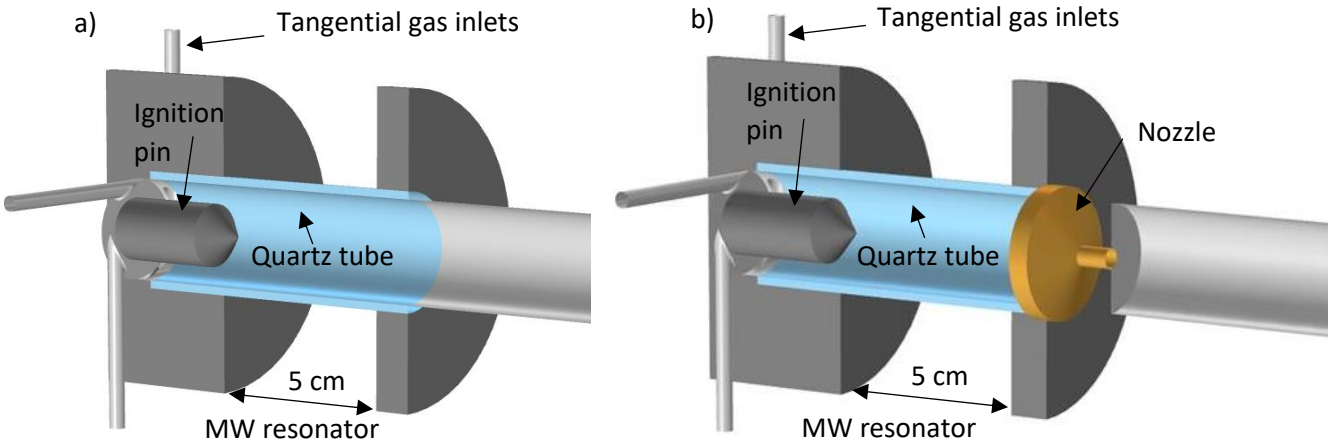

Figure 1: 3D model geometry of the MW reactor a) without and b) with nozzle attached, as described by Hecimovic et al.[1]

The gas flow behavior is described using a Reynolds-Averaged Navier Stokes (RANS) Shear Stress Transport (SST) turbulent gas flow model that solves the following mass continuity and momentum continuity equations for a Newtonian fluid.

$$\nabla \cdot (\rho_g \overrightarrow{u_g}) = 0 \quad (1)$$

$$\rho_g(\overrightarrow{u_g} \cdot \nabla)\overrightarrow{u_g} = \nabla \cdot \left[-p\vec{I} + (\mu + \mu_T)\left(\nabla\overrightarrow{u_g} + \nabla(\overrightarrow{u_g})^T\right) - \frac{2}{3}(\mu + \mu_T)(\nabla \cdot \overrightarrow{u_g})\vec{I} - \frac{2}{3}\rho_g k\vec{I}\right] + \vec{F} \quad (2)$$

where ρ_g stands for the gas density, $\overrightarrow{u_g}$ is the gas flow velocity vector, superscript T stands for transposition, p is the gas pressure, μ is the dynamic viscosity, and μ_T the turbulent viscosity of the fluid, k is the turbulent kinetic energy, $\vec{I}$ the unity tensor and $\vec{F}$ the body force vector (which includes forces like gravity or surface tension, but is considered zero as they are not the driving force of the fluid flow in this model). Note that this equation does not contain time derivatives, as the model is

solved for steady state flow, i.e. $\frac{\partial \vec{u}}{\partial t} = 0$. More information on the turbulent gas flow model and the equations for calculating k and μ_T are given in the SI (section S.2).

The gas temperature is calculated by representing the plasma as a heat source Q, using the following thermal balance equation:

$$\rho_g C_p \vec{u}_g \cdot \nabla \mathrm{T} + \nabla \cdot \vec{q}_{cond} = Q \tag{3}$$

Where ρ_g stands for the gas density, C_p for the isobaric heat capacity, T is the temperature, $\vec{u}_g$ the gas velocity field vector, and $\vec{q}_{cond}$ the conductive heat flux vector, which is calculated by:[17]

$$\vec{q}_{cond} = -(k_g + k_{g,T})\nabla T \tag{4}$$

Where k_g is the thermal conductivity and $k_{g,T}$ is the turbulent thermal conductivity of the gas, calculated by:

$$k_{g,T} = \frac{C_p \mu_T}{Pr_T} \tag{5}$$

In which μ_T is the turbulent dynamic viscosity, which is discussed more in detail in the SI (section S.2) and Pr_T the turbulent Prandtl number, as calculated by the Kays-Crawford model.[18] The material properties μ, C_p and k_g in equation 2, 3 and 4, respectively, are adopted from the work of Magin et al.[19], where these properties are calculated for a wide range of temperatures assuming thermodynamic equilibrium. This assumption is further discussed in the SI (section S.5).

In equation 3, the first term ($\rho_g C_p \vec{u}_g \cdot \nabla \mathrm{T}$) accounts for convective cooling and the second term ($\nabla \cdot \vec{q}_{cond}$) accounts for conductive cooling. While the second term directly yields the conductive heat flux $\vec{q}_{cond}$, as defined in equation 4, the convective heat flux is calculated using:

$$\vec{q}_{conv} = \rho_g \vec{u}_g \left(H - \frac{p}{\rho_g} \right) \tag{6}$$

In which the $\left(H - \frac{p}{\rho_g} \right)$ term represents the internal energy and H is the enthalpy, related to C_p through:

$$\left(\frac{\partial H}{\partial T} \right)_T = C_p \tag{7}$$

The total heat flux is then described by:

$$\vec{q}_{tot} = \vec{q}_{cond} + \vec{q}_{conv} \tag{8}$$

The final term in equation 3 (Q) accounts for the absorbed MW power that is converted into gas heating. As atmospheric pressure MW plasmas are known for very fast vibrational-translational relaxation, making them quasi-thermal or "warm" plasmas,[12,20] it is reasonable to assume that the absorbed MW power is nearly fully transferred to gas heating , which allows the integrated value of Q to be calculated using the experimental plasma power. The shape of Q, which represents the shape of the plasma, is defined using plasma measurements performed by D'Isa et al.[10] and Wolf et al.[12], who described in great detail the radial and axial profile of contracted plasma filaments in a MW reactor. A detailed description of the heat source term is given in the SI (section S.6).

2.2 Calculating the underlying chemistry in a quasi-1D chemical kinetics model

To reveal the underlying chemistry at different locations in the reactor, we developed a chemical kinetics model that simulates the CO_2 chemistry over a one-dimensional straight line in the reactor. While the model calculates the density evolution of the most important plasma species solely as a function of time, like a 0D model, it uses the spatial profile of the calculated gas temperature and gas flow velocity from the 3D CFD model as input, resulting in a quasi-1D simulation. The spatial gas flow velocity profiles that are used to make the conversion between a time-based and quasi-1D simulation are shown in the SI (section S.3). The evolution of the species densities as a function of time is described by:

$$\frac{\partial \mathrm{c_i}}{\partial \mathrm{t}} = \sum_j \mathrm{a}_{ij} r_j \tag{9}$$

in which c_i is the concentration of species *i* (mol.m^{-3}), and j is the index for the reactions included in the model. The stoichiometric coefficients are denoted as a_{ij}, and are defined as being negative for reactants and positive for products. The reaction rates (r_j, mol/(m^3·s)$^{-1}$) can be described by the mass action law:

$$r_j = k_j^f \prod_\mathrm{i} \mathrm{c_i}^{-\mathrm{a}_{ij}} - k_j^r \prod_\mathrm{i} \mathrm{c_i}^{\mathrm{a}_{ij}} \tag{10}$$

Here, k_j^f and k_j^r represent the forward and reverse rate coefficients, respectively. The reactions included in the model are shown in *Table 1*. This set only includes thermal reactions of species that play a significant role in the thermal dissociation and recombination pathway of CO_2. The rate coefficients of the forward reactions, shown in *Table 1*, are taken from the Gri-mech 3.0 database,[21] while the rate coefficients of the reverse reactions are calculated assuming thermodynamic equilibrium:

$$k^r = \frac{k^f}{K_{eq}} \tag{11}$$

In which K_{eq} is the equilibrium constant of the reaction, calculated using thermodynamic constants of the NASA-Glenn database.[22]

Table 1: List of reactions and reaction rate coefficients of the forward reactions used in the model, as adopted from the Gri-mech 3.0 database.[21] The rate coefficients of the backward reactions are calculated assuming thermodynamic equilibrium. M in the reactions below represents any neutral species, R is defined as 8.314 J(K.mol)$^{-1}$, c_M is given in mol.cm^{-3}, and T in K.

Reaction	Reaction rate coefficient of forward reaction
$CO + O + M \rightleftarrows CO_2 + M$	$k = \frac{k_{inf}}{\frac{1 + k_{inf}}{k_o c_M}}$ $k_{inf} = 1.80 \times 10^{10}\ [\mathrm{cm^3 mol^{-1} s^{-1}}] \exp\left(\frac{-9978.8\ [\frac{J}{mol}]}{RT}\right)$ $k_o = 6.02 \times 10^{14}\ [\mathrm{cm^6 mol^{-2} s^{-1}}] \exp\left(\frac{-12552\ [\frac{J}{mol}]}{RT}\right)$
$CO + O_2 \rightleftarrows CO_2 + O$	$k = 2.50 \times 10^{12}\ [\mathrm{cm^3 mol^{-1} s^{-1}}] \exp\left(\frac{-2 \times 10^5 [\frac{J}{mol}]}{RT}\right)$
$O + O + M \rightleftarrows O_2 + M$	$k = \frac{1.20 \times 10^{17}\ [\mathrm{cm^6 mol^{-2} s^{-1}}]}{T}\ c_M$
$C + O + M \rightleftarrows CO + M$	$k = 7.76 \times 10^6\ [\mathrm{cm^6 mol^{-2} s^{-1}}] \left(\frac{T}{300\ [K]}\right)^{-3.08} \exp\left(\frac{-2114\ [K]}{T}\right) c_M$

3. Results and discussion

3.1 Experimental performance of the nozzle

Figure 2 presents the experimental results acquired by Hecimovic et al.[1], showing the conversion as a function of the input flow rate in the MW reactor without and with nozzles of varying diameters, for a plasma power of 1500 W and an operating pressure of 900 mbar (which, as mentioned, is representative for atmospheric pressure operating conditions). In addition, the inverse relation between flow rate and conversion, that holds in the case of constant energy efficiency, is marked with a grey dashed line. In general, figure 2 shows a significantly higher conversion and energy efficiency when a nozzle is attached to the reactor. Interestingly, the performance enhancement of the nozzle is most significant at lower flow rates: while the rise in conversion at 20 slm is only a few % for a nozzle with diameter of 2.5 mm, at 5 slm the same nozzle enhances the conversion by a factor 7, i.e., from 5 to 35 %. Furthermore, the best improvements are observed at smaller diameter nozzles. Through computational modelling we aim to fully explain these trends and identify the quenching mechanisms of the nozzle, using the following steps: in section 3.2, we simulate the gas flow and heat transfer inside the MW reactor without nozzle attached as a reference case, varying the gas input flow rates as shown by the black datapoints in figure 2. Subsequently, in section 3.3 we describe the gas flow and heat transfer inside the MW reactor with a nozzle attached at different input flow rates and different nozzle diameters, as shown by the blue datapoints in figure 2. Then, in section 3.4 we validate our model results to experimental temperature data, measured using optical emissions spectroscopy (OES). Finally, in section 3.5, using the calculated temperature data from these 3D models, we describe the

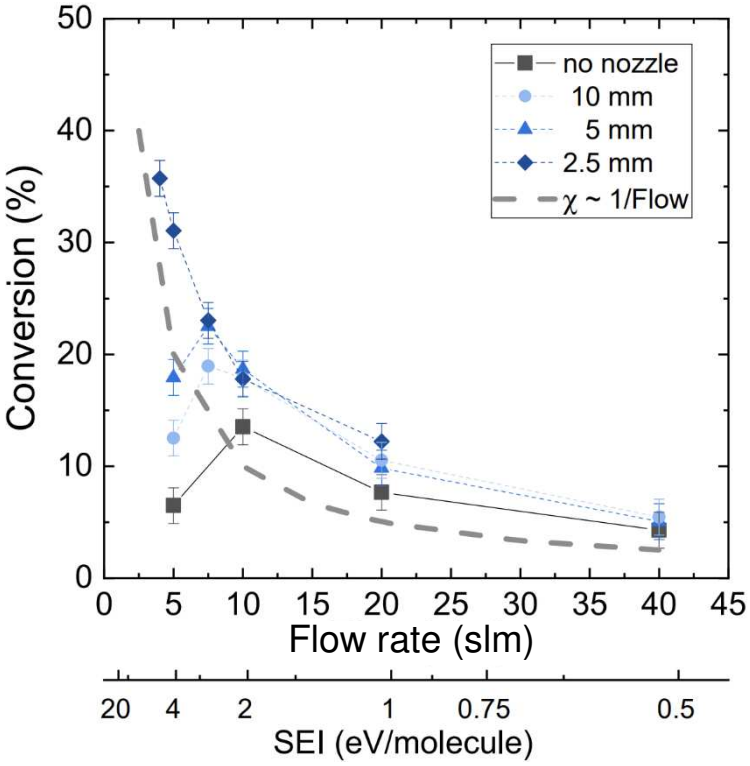

Figure 2: Measured conversion in the MW CO_2 plasma as a function of flow rate and SEI. The black line represents conversion without the nozzle, and the blue symbols are for different nozzle diameters, as indicated in the legend. The gray dashed line indicates the inverse relation between conversion and flow rate. The operating pressure is 900 mbar and the plasma power is 1500 W.

effect of the nozzle on the recombination reactions and the net conversion, using a quasi-1D chemical kinetics model.

3.2 Behavior of the MW reactor without nozzle

The flow pattern inside the MW reactor, as calculated by our 3D CFD model, is shown in figure 3. The figure shows that the tangential gas injection creates a swirling gas flow in the reactor, which results in two distinct regions in the reactor, i.e. a cold edge and a hot center: gas swirling near the reactor walls flows at a high gas flow velocity around the hot plasma filament (indicated in the figure by the red cone), thus remaining cold and untreated by the plasma. This cool, high velocity swirling gas flow is vital to stabilize the plasma in the center of the reactor and to shield the quartz tube walls from overheating. Gas near the center of the reactor swirls at a lower flow velocity and is heated by the plasma filament (red cone) that is formed above the ignition pin. The gas temperature in this region increases significantly towards the center of the reactor, reaching temperatures up to 6000 K for gas flowing through the core of the plasma filament (see below).

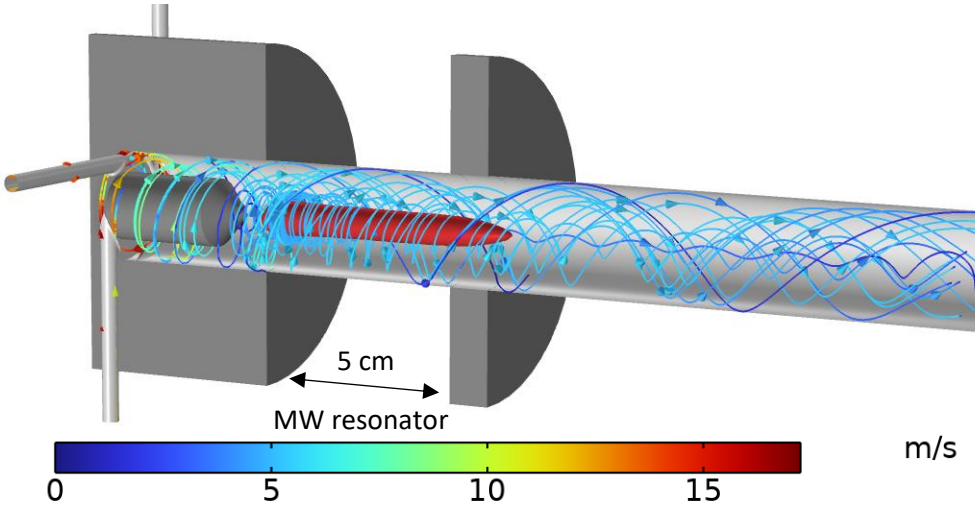

Figure 3: Calculated gas flow velocity streamlines in the MW reactor without a nozzle attached, operating at a flow rate of 20 slm and a pressure of 900 mbar. The contracted plasma filament is schematically illustrated in red.

Figure 4 illustrates the calculated gas temperature profiles inside the MW reactor operating at different flow rates. As the flow rate increases, the core plasma temperature remains more or less the same, i.e. between 5500-6000 K, which is in good agreement with the axial temperature profiles measured OES, which are discussed further in section 3.4. The shape and temperature of the afterglow, however, strongly change upon increasing flow rate, resulting in a cooler, narrower and shorter afterglow upon higher flow rates.

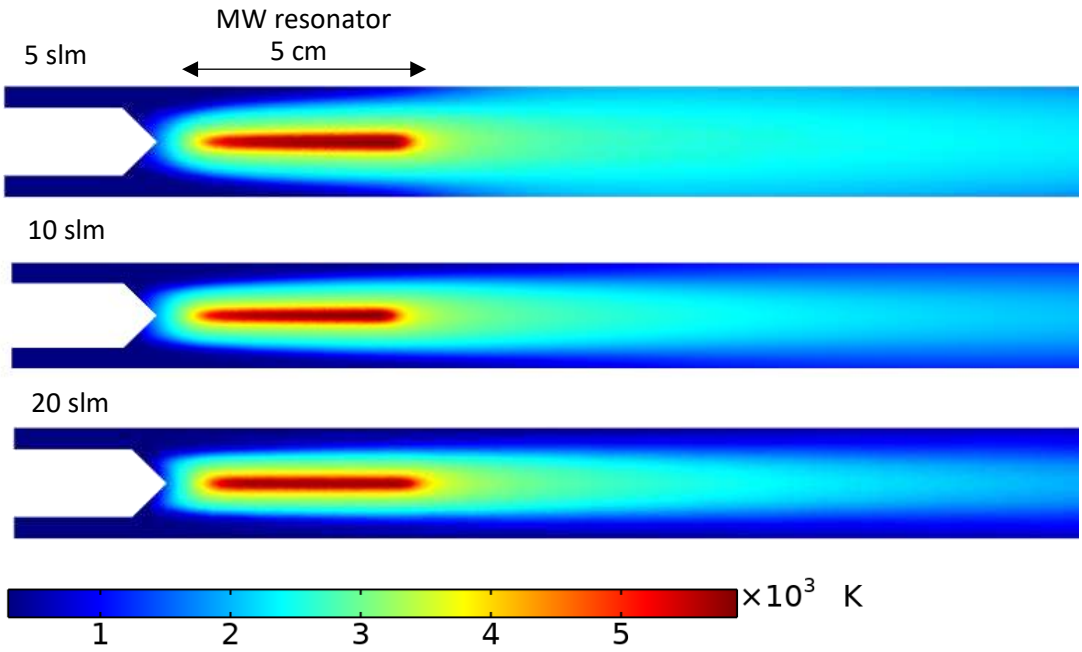

Figure 4: Calculated temperature profiles in the MW reactor without a nozzle attached, for flow rates of 5, 10 and 20 slm, operating at a pressure of 900 mbar and a plasma power of 1500 W

Figure 5 presents the magnitude and the direction of the calculated heat flux (as defined in equation 4, 6 and 8) at the different flow rates, while outlining the shape of the plasma filament in black. The direction of the convective cooling is represented by the black arrows, while the direction of the conductive cooling is represented by the red arrows. The figure shows that the cooling gradually increases upon higher flow rate, as the most significant cooling present is convective cooling, which increases at higher flow rates. The model shows that conductive cooling also occurs near the edges of the plasma filament where the highest temperature gradient is present (as indicated by the red arrows), but this cooling is an order of magnitude lower than the convective cooling of the gas flow. The figure clearly demonstrates that little heat transfer is present between the hot plasma core and the cool periphery gas flow around the plasma, due to the lack of mixing between these two regions. Given the increased convective cooling inherently present at higher flow rates, these higher flow rates tend to more effectively quench recombination reactions, which destroy the formed CO in the plasma afterglow. This will be further explained in section 3.5.

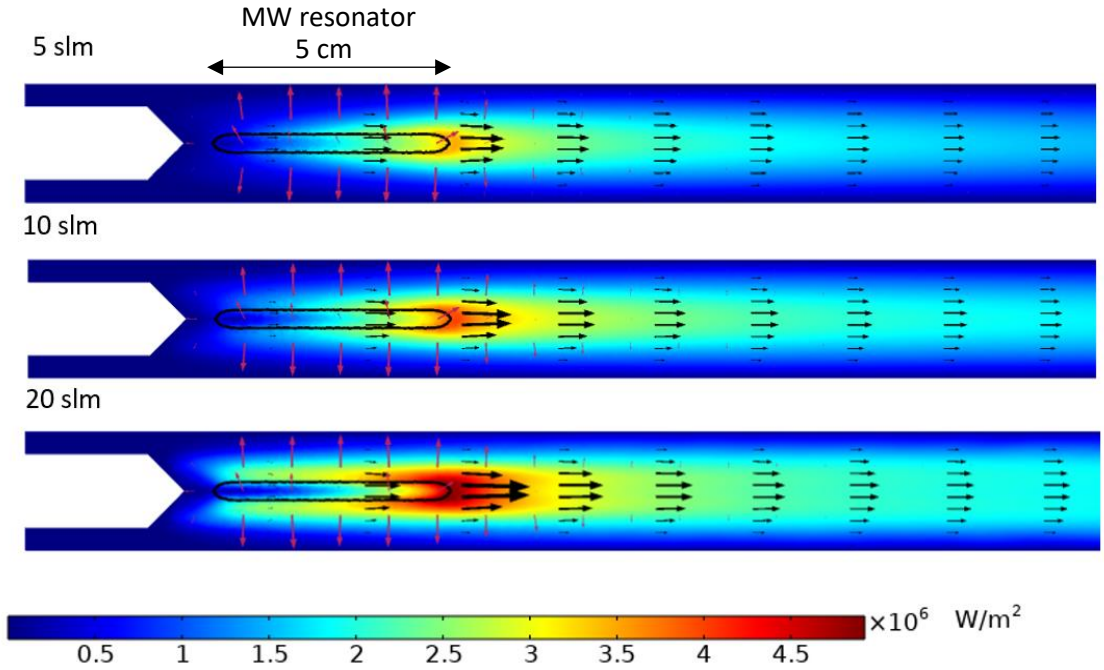

Figure 5: Calculated heat flux magnitude profile in the MW reactor without a nozzle attached, for flow rates of 5, 10 and 20 slm, operating at a pressure of 900 mbar and a plasma power of 1500 W. The direction of the convective heat flux is represented by the black arrows, while the direction of the conductive heat flux is represented by the red arrows. The shape of the plasma filament is outlined in black.

3.3 Revealing the effect of the nozzle

When a nozzle is attached in the reactor's effluent, the flow pattern in the reactor significantly changes, as shown by the calculated streamlines in figure 6 a). This figure demonstrates that the nozzle disturbs the swirling flow pattern, forcing the rotating flow to converge and mix the hot gas in the center with the cool periphery gas flow, right at the end of the plasma. The flow is then highly accelerated by the small opening in the nozzle. Figure 6 b) shows the same calculated streamlines as figure 6a) but using the color scale of figure 3, for an easy comparison of the flow behavior between a reactor with and without nozzle attached. As discussed and shown more clearly in section 3.5, the influence of the nozzle on the flow is already present before the gas has reached the nozzle, as the converging movement of the gas is dragged upstream by the gas viscosity. This causes a slight increase in gas flow velocity in the center of the reactor already before the nozzle when a nozzle is attached.

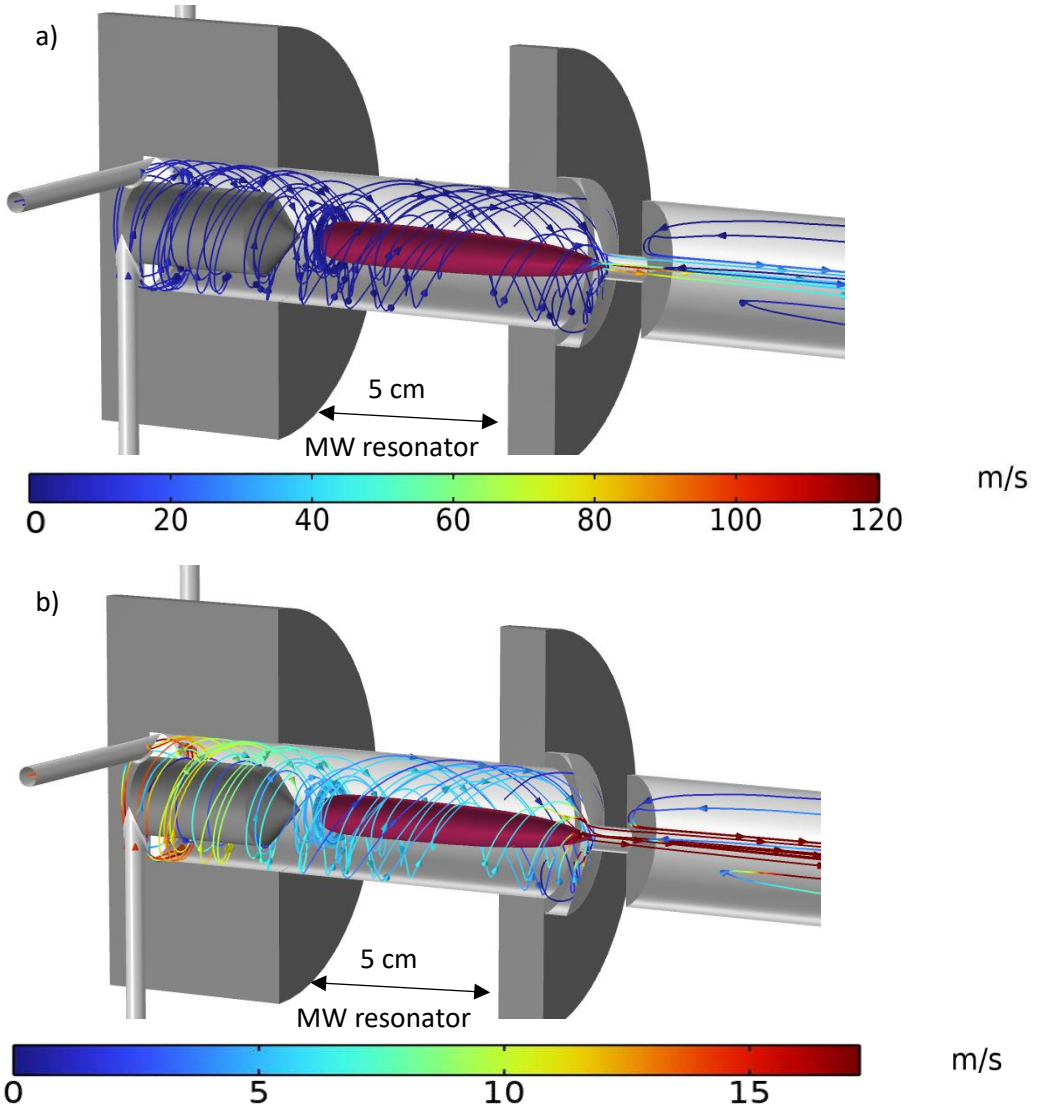

Figure 6: Calculated gas velocity streamlines in the MW reactor with a 5 mm nozzle attached, operating at a flow rate of 20 slm and a pressure of 900 mbar. The plasma filament is schematically illustrated in red. Figure b shows the same streamlines as figure a, but with the color scale of figure 3, to allow easy comparison between a reactor with and without nozzle.

The effect of the nozzle on the temperature profile in the plasma torch when using the nozzle is presented in Figure 7 , where the calculated temperature profile in the reactor with a 5 mm nozzle for different flow rates is shown. It is clear that the nozzle greatly affects the temperature in the afterglow, which drops by more than 4000 K compared to the plasma region, and is different for the different flow rates. Again, good agreement is reached between the calculated temperature profiles and the experimentally measured temperatures, which will be discussed further in section 3.4. Compared to figure 4, the plasma's hot afterglow is significantly shortened: after the nozzle, the gas temperature quickly cools down below 2000 K. Similar to the reactor without nozzle, the fastest cooling is observed at the higher flow rate, which will be discussed in more detail in section 3.5.

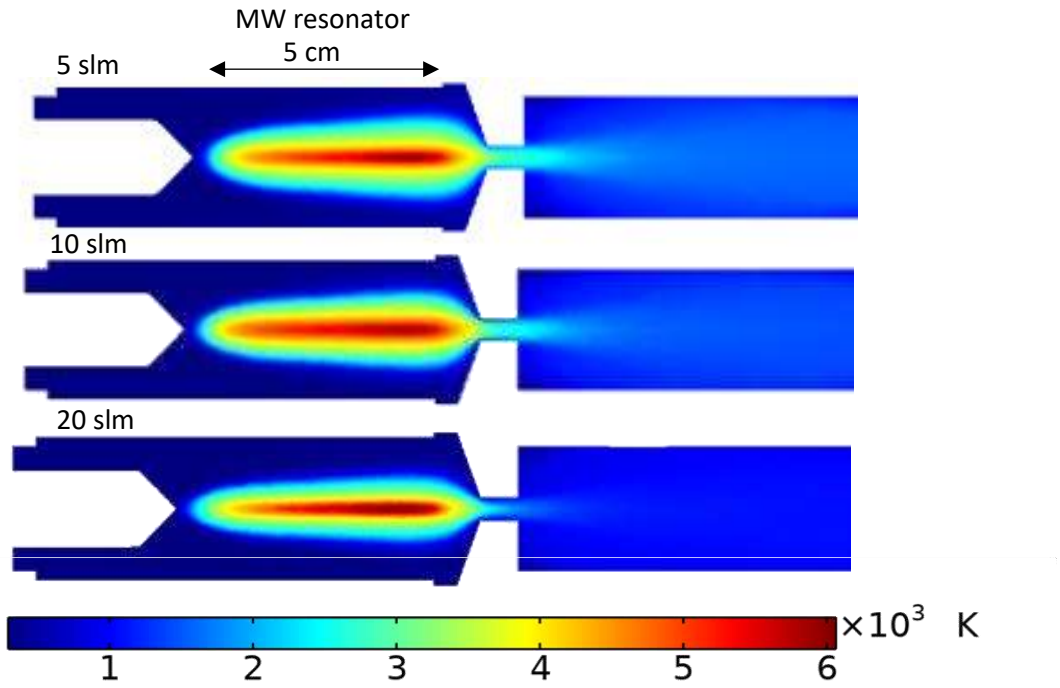

Figure 7: Calculated temperature profiles in the MW reactor with a 5 mm nozzle attached, for a flow rate of 5, 10 and 20 slm, operating at a pressure of 900 mbar and a plasma power of 1500 W

The heat transfer in the plasma torch with the nozzle becomes very concentrated in the throat of the nozzle as shown in Figure 8 which shows the magnitude and direction of the calculated heat flux in the MW reactor with 5 mm nozzle for different flow rates. The black arrows represent the direction of the convective heat flux and the red arrows the direction of the conductive heat flux. Compared to figure 5, the heat flux magnitude has increased by two orders of magnitude and is now mainly located in the throat of the nozzle. Our model shows that the cooling effect of the nozzle has two origins. First, the nozzle forces the cool, untreated gas near the walls to mix with the hot gas in the center. The second effect is due to the nozzle itself being externally cooled with cooling water. This is primarily done to prevent the copper nozzle from melting, as it is placed close to the hot plasma, but the model shows that, in addition, this greatly enhances the quenching capabilities of the nozzle. The effect of the cooled nozzle is demonstrated in figure 9, comparing the axial temperature profile in the center of the MW reactor between a 5 mm nozzle, cooled by room temperature water, and a hypothetical case where the nozzle is not cooled (and the heat loss is only defined by the limited heat dissipation through the reactor walls, like the rest of the reactor walls), for (a) a flow rate of 5 slm and (b) a flow rate of 20 slm. For both flow rates the figure shows that both nozzles display a very similar cooling curve, but the cooled nozzle allows to eventually reach a temperature that is slightly lower (i.e. -500 K for 5 slm and -300 K for 20 slm) than the nozzle without water cooling. Hence, in addition to the convective cooling resulting from gas mixing inside the nozzle, conductive cooling through the nozzle walls allows for a significant portion of heat (i.e. ca. 275 W for 5 slm and 200 W for 20 slm) to be transferred out of the system, thus reaching lower overall temperatures in the afterglow. Note that more heat is transferred at 5 slm, as the lower flow rate allows the gas to spend more time in contact with the nozzle, resulting in more time to exchange heat with the cooled nozzle walls. Surface integration of the total calculated heat flux across the nozzle walls shows that the conductive cooling through the nozzle walls increases the overall heat transfer, and thus the overall cooling capacity of the nozzle, by ca. 35%. As illustrated by figure 9 a), the temperature would remain around 2500 K if no cooling is applied in the 5 slm regime, but it lowers to below 2000 K when the nozzle is cooled. As will be shown in section 3.5, this is an important temperature threshold for the recombination chemistry that is reached thanks to the nozzle

cooling. In the 20 slm regime, however, figure 9 b) demonstrates that the temperature reaches the 2000 K threshold either way, both when the nozzle is and isn't cooled, thanks to the increased convective cooling present at this higher flow rate. Hence, the fact that the nozzle walls are cooled is expected only to influence the CO retention at lower flow rates (i.e. 5 slm).

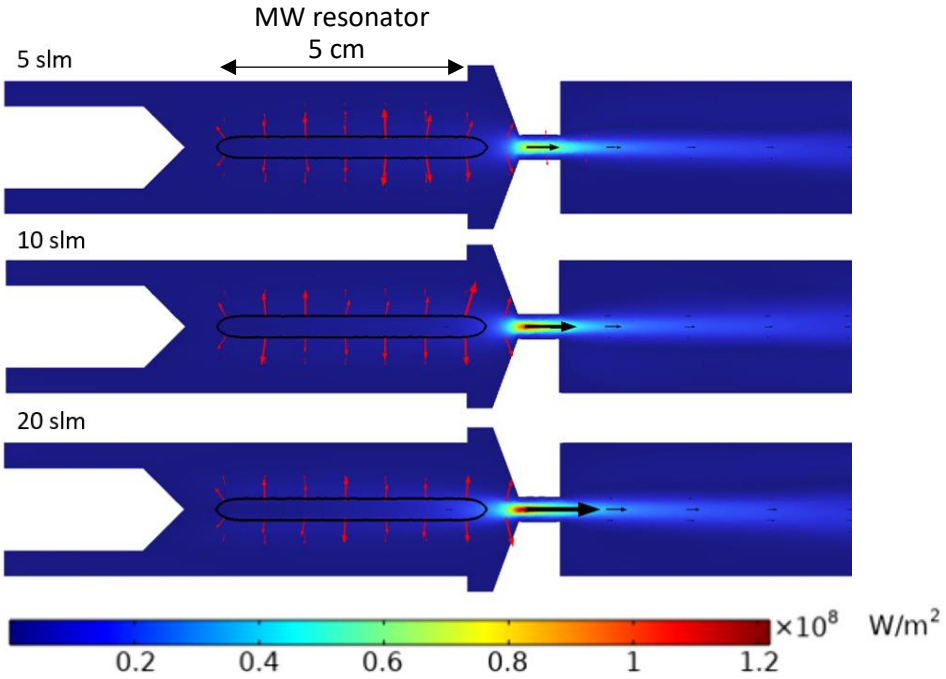

Figure 8: Calculated heat flux magnitude profile in the MW reactor with a 5 mm nozzle attached, for a flow rate of 5, 10 and 20 slm , operating at a pressure of 900 mbar and a plasma power of 1500 W. The direction of the convective heat flux is represented by the black arrows, while the direction of the conductive heat flux is represented by the red arrows. The shape of the plasma filament is outlined in black.

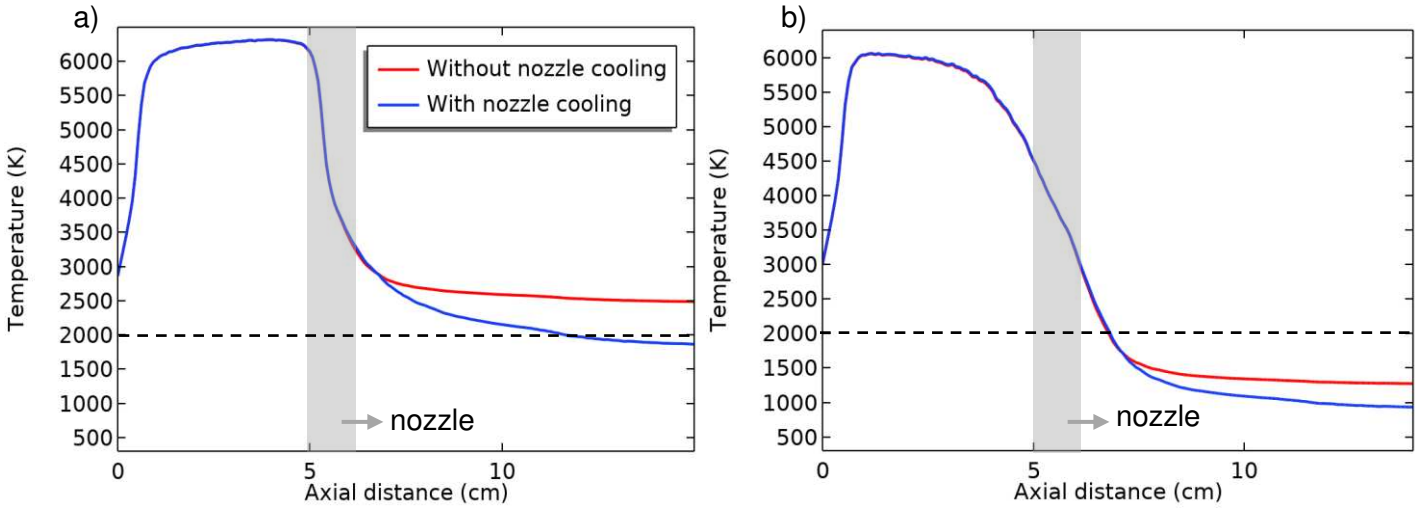

Figure 9: Calculated axial temperature profile in the center of the MW reactor for a reactor quipped with a cooled 5 mm nozzle attached and for a hypothetical case when the nozzle isn't cooled, for a) a flow rate of 5 slm and b) a flow rate of 20 slml

Finally, the magnitude of the heat transfer is also influenced by the nozzle diameter. Figure 10 shows the magnitude and direction of the calculated heat flux with nozzles of different diameters attached to a reactor operating at 10 slm. The black arrows represent the direction of the convective heat flux and the red arrows the direction of the conductive heat flux. As the nozzle diameter decreases, the

cooling effect of the nozzle increases. Forcing the gas through a smaller opening induces more gas mixing and higher gas flow velocities, which increases convective cooling. Furthermore, it also induces more contact with the cooled nozzle walls, resulting in more conductive cooling. Note that reducing the nozzle diameter yields a higher pressure inside the reactor. The thermal expansion of the hot gas within the plasma induces a high gas flow throughout the reactor. While a reactor without nozzle attached can sustain this high flow rate without a local pressure increase, the constriction of the nozzle is too narrow to maintain the pressure of 900 mbar in the reactor. This is illustrated in figure 11, displaying the calculated pressure profiles in a reactor, a) without and b) with a 2.5 mm nozzle attached, operating at a flow rate of 10 slm. The model predicts the pressure difference over the nozzle (i.e. before and after the narrow nozzle gap) to be about 250 mbar, which is comparable to the pressure differences observed experimentally by Hecimovic et al.[1] In the simulation the pressure difference was observed as the increase of the pressure in the resonator, with respect to the 900 mbar boundary conditions in the effluent. In the experiment the 900 mbar were maintained inside the resonator and the low pressures are observed in the effluent. This difference between modelling and experiment is not expected to affect the results, as around atmospheric pressure, the plasma chemistry and CO_2 conversion in MW plasmas has shown to be insensitive to moderate pressure changes.[1,15] While this pressure build-up is not enough to yield supersonic flow velocities, we can expect this to occur when the pressure on the outlet is reduced below 900 mbar. Figure 11 b) also illustrates the flow pattern after the nozzle, using arrows that represent the direction of the flow velocity vector. After the gas flows out of the narrow nozzle at high gas flow velocities, part of the gas recirculates back once its velocity is decreased. This effect might further aid the heat transfer after the cooling nozzle by mixing the gas. However, the most significant cooling occurs within the nozzle.

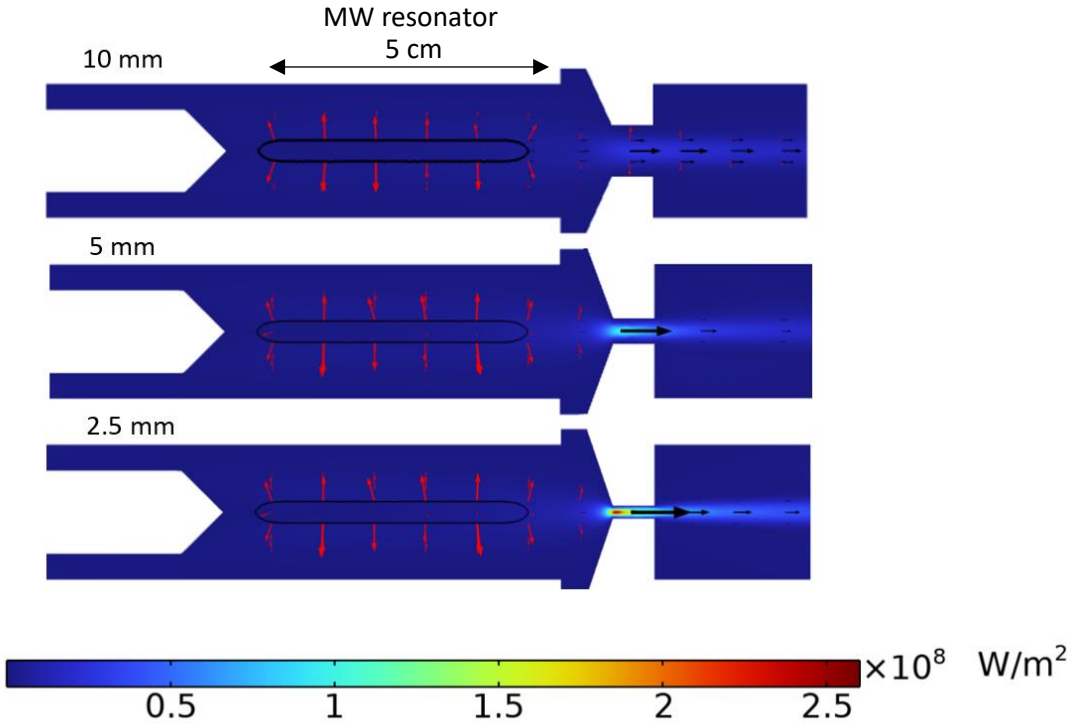

Figure 10: Calculated heat flux magnitude profile in the MW reactor with a 10, 5 and 12.5 mm nozzle attached, for a flow rate of 10 slm, operating at a pressure of 900 mbar and a plasma power of 1500 W

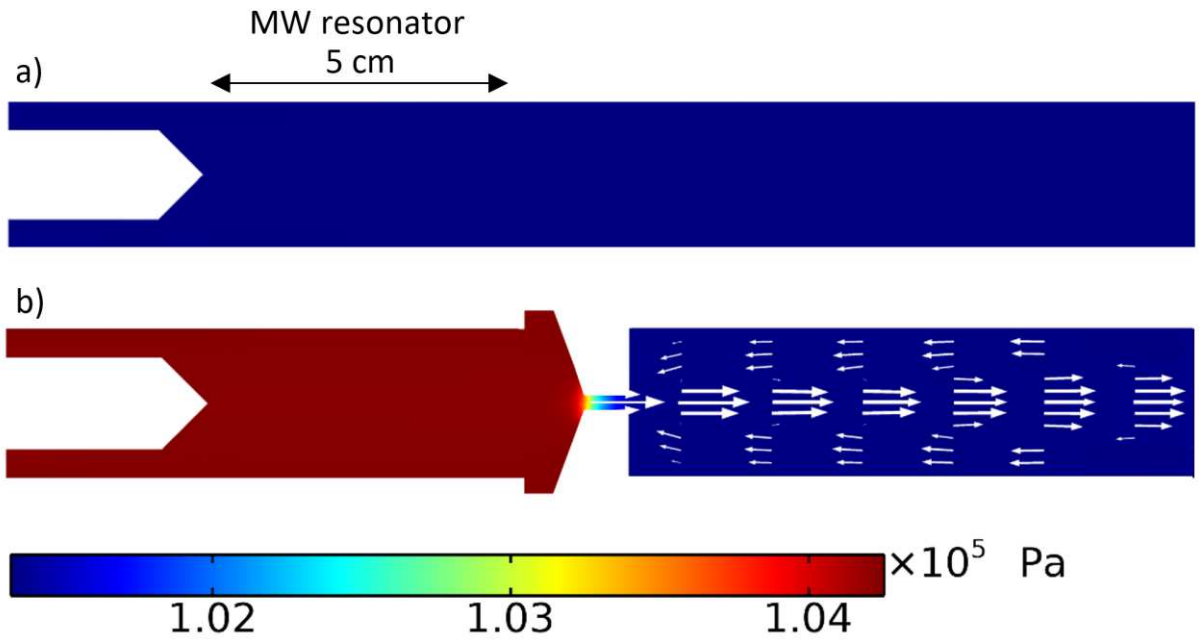

Figure 11: Calculated pressure profile in a reactor operating at 10 slm a) without and b) with a 2.5 mm nozzle attached. The recirculation zone in the flow after the nozzle is illustrated by the arrows in b).

3.4 Validation of the calculated gas temperature profiles

Figure 12(a) presents the axial profile of the gas temperature in the plasma, measured using OES (C_2 Swan band) by D'Isa et al.,[10] as well as the gas temperature calculated by our 3D CFD model for a MW reactor without a nozzle, operating at a flow rate of 10 slm. Figure 12(b) presents the same data for a MW reactor with a 2.5 mm nozzle attached, and in addition shows the axial profile of the vibrational temperature, also measured using OES, making use of the database developed by Carbone et al.[23] Figure 12(b) shows that the MW plasma is in quasi-thermal equilibrium, as the vibrational temperature is more or less equal to the gas temperature. Furthermore, the figures show that the gas temperature calculated by the model is in satisfying agreement with the experimental data.

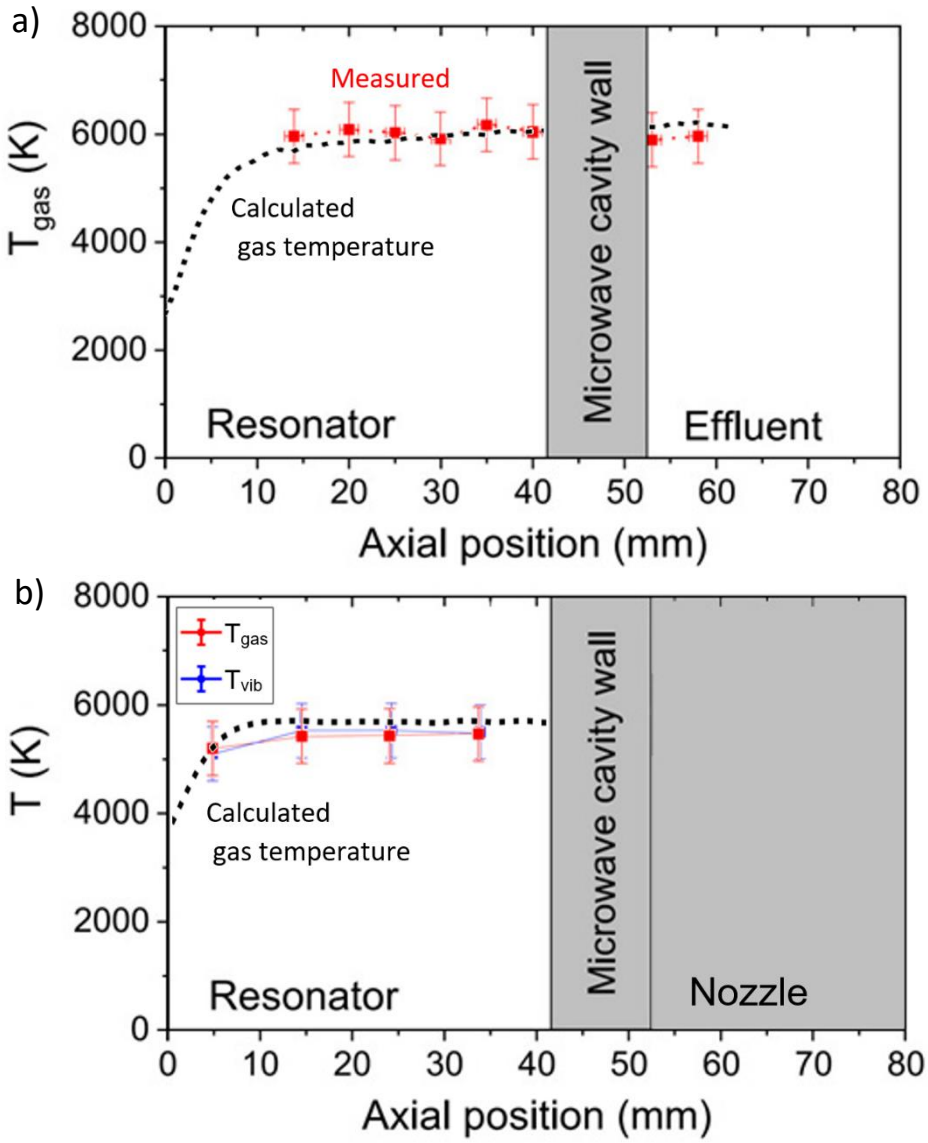

Figure 12: Axial profile of the measured gas (rotational) temperature, as well as the gas temperature calculated by our 3D CFD model, for a MW reactor, a) without nozzle attached, as adopted from D'Isa et al.[10] and b) with a 2.5 mm nozzle attached, operating at 10 slm, at a pressure of 900 mbar and a plasma power of 1500 W. In (b), also the vibrational temperature is plotted.

Figure 13 presents the radial temperature profiles of the calculated gas temperatures and the gas temperature measured with a thermocouple at different distances from the waveguide, for a MW reactor with 5 mm nozzle, operating at different flow rates. Note that at lower flow rates, the temperature could only be measured at longer distances from the waveguide due to the temperature becoming too high for thermocouple measurements. The figures displays satisfying agreement between the calculated gas temperatures and the experimental data.

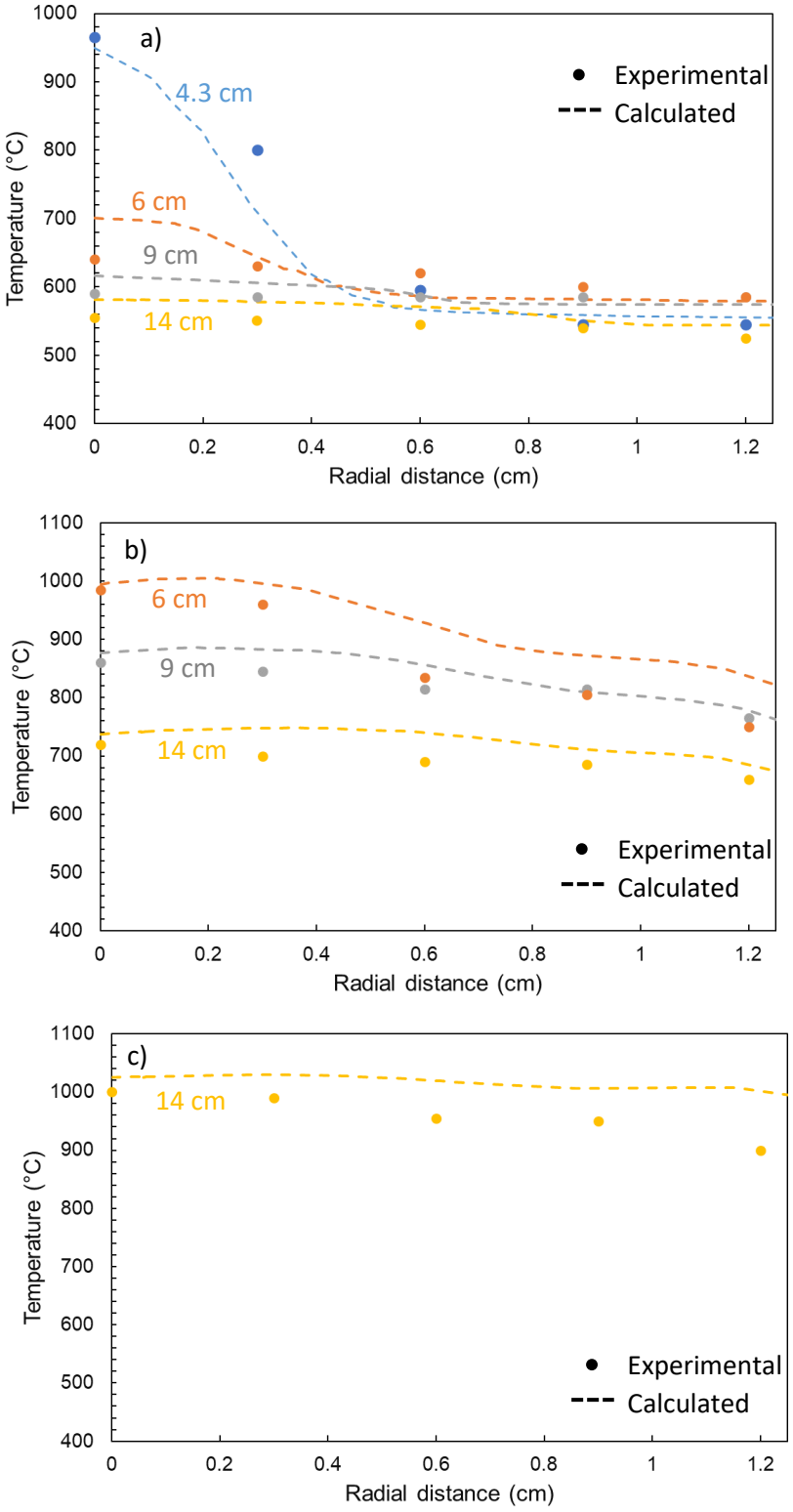

Figure 13: Calculated and experimental radial temperature profiles at different distances from the waveguide, for a MW reactor with a 5 mm nozzle attached, for a flow rate of a) 20 slm, b) 10 slm and c) 5 slm, at a pressure of 900 mbar and a plasma power of 1500 W.

3.5 Effect on the conversion and underlying chemistry

In this section we reveal how the cooling capabilities of the nozzle affect the recombination reactions and why this quenching effect is more significant for lower flow rates. To investigate the mechanisms of the CO recombination reactions and to reveal important temperature thresholds in the thermal CO_2 dissociation process, we modeled the CO_2 chemistry in the reactor with a quasi-1D chemical kinetics model. This model simulates the thermal CO_2 dissociation process over a one-dimensional straight line in the reactor, based on the gas flow velocity and temperature profile, as calculated by the 3D CFD model. Figure 14 shows the result of the quasi-1D chemical kinetics model for a reactor operating at a flow rate of 20 slm without nozzle, for a temperature profile taken in the center of the reactor. These simulation results thus represent the evolution of gas flowing through the center of the plasma filament, starting at the beginning of the waveguide. The left y-axis of figure 14 corresponds to the gas temperature profile, illustrating that in the plasma core the gas heats up to 6000 K, but at the end of the waveguide (corresponding to 0.17 s), the gas quickly cools back down, to 1500 K after 0.23 s. The right y-axis of figure 14 shows the corresponding calculated CO production rate. A positive value for the production rate indicates the formation of CO (mainly by the $CO_2 + O \rightarrow CO + O_2$ reaction), while a negative value for the formation rate indicates the destruction of CO (mainly by the $CO + O + M \rightarrow CO_2 + M$ reaction).

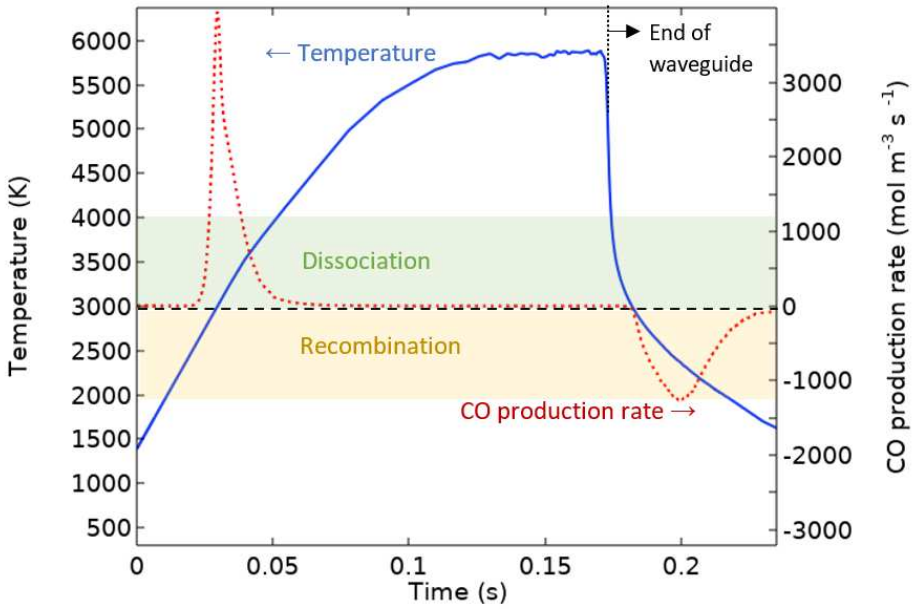

Figure 14: Calculated gas temperature profile (left y-axis) and CO production rate (right y-axis) over a straight line in the center of the MW reactor without a nozzle attached, for a flow rate of 20 slm. The temperature threshold for net thermal CO_2 dissociation above 3000 K and the zone of recombination between 2000 and 3000 K are also highlighted in the figure.

The figure shows that as the gas approaches the plasma filament and the gas temperature rises above 1800-2000 K, the formation rate of CO increases, eventually reaching a peak value around a temperature of 3000 K. As highlighted in the figure, this temperature value is considered the threshold for efficient thermal CO_2 conversion. While the exact values of these temperature thresholds can vary slightly upon changing flow rate, they are in good agreement with what is expected in literature for thermal CO_2 chemistry at atmospheric pressure.[4] Once the gas temperature increases further, the CO formation rate decreases again, eventually reaching zero at around 0.05 s, when the temperature has reached ca. 4000 K. At these temperatures the rate of CO recombination balances the dissociation rate, reaching a steady state situation where there is no net formation or destruction of CO. Note that at

temperatures around 6000 K, CO dissociation into C and O is also present, although in a very limited amount. Once the gas has passed through the plasma filament and cools back down to below the 3000 K threshold, the efficient thermal CO_2 dissociation diminishes, while the recombination reactions still occur. This translates into a negative CO formation rate, because CO recombines with O (+ M) into CO_2 (+ M). Hence, 3000 K is considered the threshold for the recombination reactions (as indicated by the horizontal dashed line in figure 14). Once the gas temperature decreases below ca. 2000 K, the CO formation rates becomes zero again, as the temperature is now too low for either of the recombination or dissociation reactions to occur. To avoid recombination reactions and reduce the overall CO destruction, the gas temperature should thus, once cooled down below the 3000 K threshold, drop as quickly as possible below 2000 K to quench the recombination reactions. Integration of the positive and negative CO production peaks in figure 14 shows that the time-integrated CO destruction rate is 72 % of the time-integrated CO production rate, meaning that 72 % of the CO that is formed in the center of the plasma is destroyed after the plasma by recombination.

Similar to figure 14, figure 15 illustrates the calculated temperature profile and CO production rate in the center of the reactor, again for a reactor without nozzle, but operating at 5 slm. At this lower flow rate, the gas takes more time to reach the plasma filament and heat up to the 3000 K and 4000 K thresholds. Likewise, the gas spends a longer time at the temperature for net thermal conversion, making the initial CO production peak broader compared to at 20 slm, although the maximum value is clearly lower (cf. figure 15 vs. figure 14). However, after the plasma the gas also cools down more slowly, due to the limited convective cooling shown previously in figure 5. As a result, the gas also spends more time in the recombination zone below 3000 K, broadening the CO destruction peak, and resulting in a higher loss in CO due to recombination reactions. Indeed, while for a flow rate of 20 slm, 72 % of the produced CO was destroyed in the negative CO production peak in figure 14, time-integration of the CO production peaks in figure 15 shows that for a flow rate of 5 slm, 83 % of the produced CO is destroyed by recombination after the plasma.

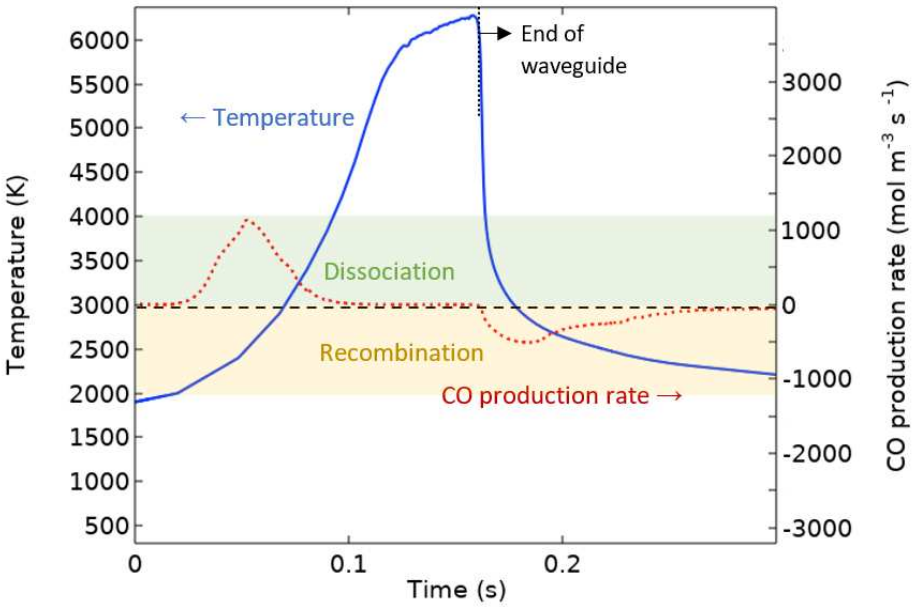

Figure 15: Calculated gas temperature profile (left y-axis) and CO production rate (right y-axis) over a straight line in the center of the MW reactor without a nozzle attached, for a flow rate of 5 slm. The temperature threshold for net thermal CO_2 dissociation above 3000 K and the zone of recombination between 2000 and 3000 K are also highlighted in the figure.

Figure 16 shows the results for running the quasi-1D chemical kinetics model in the center of the reactor for 20 slm (a) and 5 slm (b) with a 5 mm nozzle attached to the reactor. The results from figure 13 and 14 without nozzle are also depicted (as dashed lines) to more easily distinguish the effect of the nozzle. The figures show that for both high and low flow rate, adding a nozzle drastically changes the cooling curve after the plasma in two distinct ways: (i) while the temperature is slightly higher inside the plasma, it reaches a lower value after the plasma compared to when no nozzle is attached, and (ii) the average cooling rate in the effluent is much higher, i.e., it rises from 9.1×10^4 to 6.0×10^5 K/s for 20 slm, and from 6.4×10^4 to 4.8×10^5 K/s for 5 slm. Locally, in the steepest part of the cooling curve, the cooling rate even exceeds 10^7 K/s, which is indeed high enough to efficiently suppress recombination reactions according to literature.[24] Due to these high quenching rates, the time spent after the plasma in the recombination zone between 2000 and 3000 K (i.e. 0.03 s for 20 slm and 0.12 s for 5 slm) is drastically reduced compared to the reactor without quenching nozzle, especially for the 5 slm case, where the gas took a long time to cool down below 2000 K without nozzle attached. As a result, recombination only occurs for a very short time, which is represented by the very narrow negative peaks in the CO production rate. Note that these destruction peaks are high in intensity, reaching almost -10,000 mol $m^{-3}s^{-1}$ at 20 slm. This is due to the high concentration of O atoms that are still present for a short amount of time when the gas is quickly quenched from 6000 K. However, these peaks are very short in duration (i.e. less than 0.5 ms), resulting in very low overall CO recombination during this timeframe. For 20 slm, the time-integrated value of the CO destruction peaks in figure 16 (a) is reduced from 72 % to 24 % of the time-integrated CO production peak, while for 5 slm in figure 16 (b), the time-integrated CO destruction is reduced from 83 % to 64 % of the time-integrated CO production peak. Note that attaching a nozzle not only impacts the cooling curve of the temperature profile, but also has a limited influence on the heating curve: both for the 20 slm and 5 slm regime, the temperature profile reaches its maximal value slightly faster when a nozzle is attached. As mentioned earlier in section 3.3, this is attributed to the flow velocity field in the reactor that has slightly adapted to the converging shape of the nozzle, making the gas flow slightly faster in the center of the reactor.

While this reduced CO destruction due to fast quenching explains the overall improvement seen in figure 2 when the nozzle is attached, it does not yet explain the significantly higher improvement at lower flow rates compared to higher flow rates. However, figures 14 - 16 only represent gas flowing through the center of the plasma, and do not capture the overall effect in the whole reactor. Indeed, a significant portion of the treated gas will not experience the maximum temperature of 6000 K in the center of the plasma filament, but will flow closer near the edges of the plasma, where the gas temperature lies between 2000 – 4000 K.

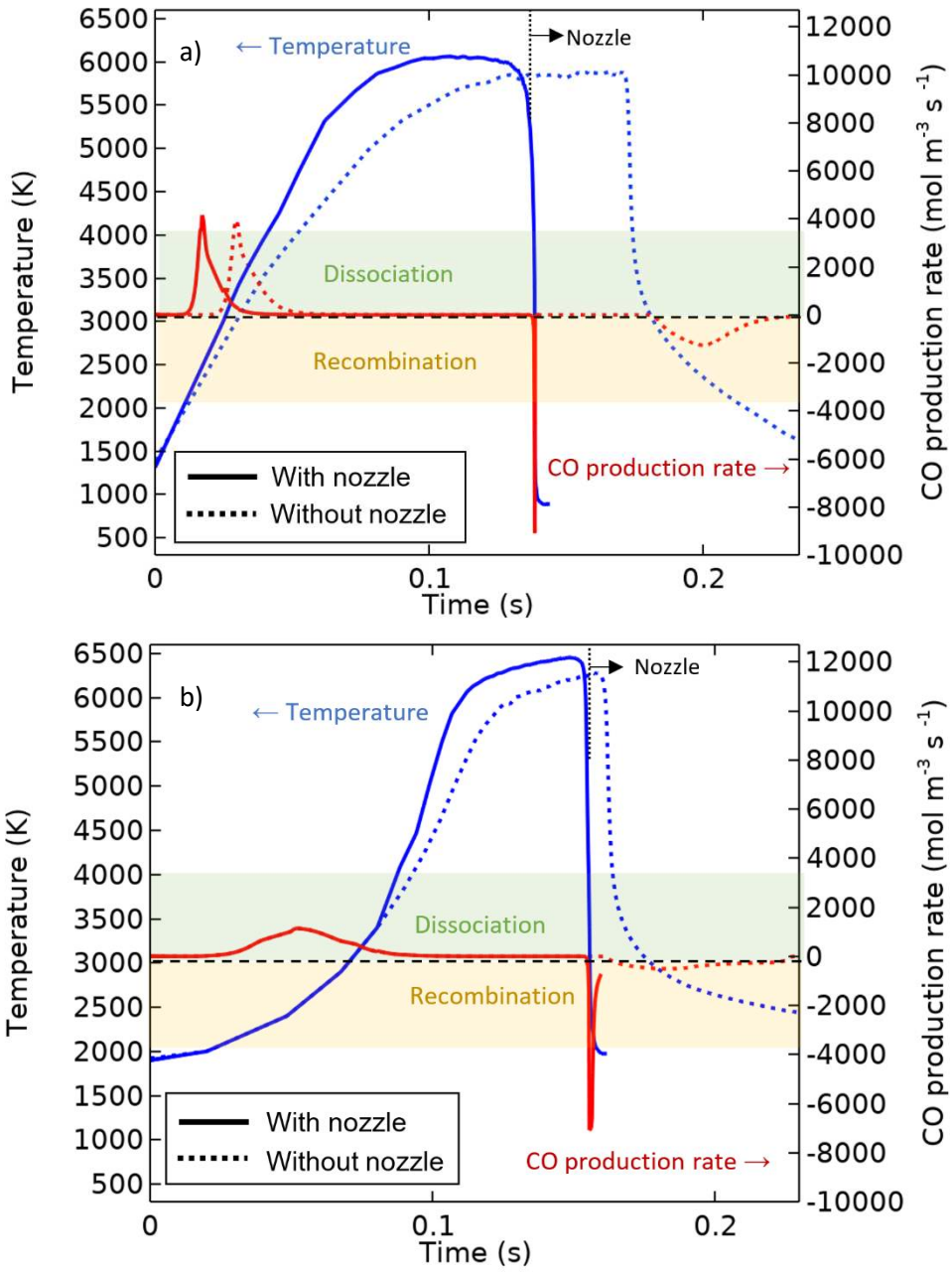

Figure 16: Calculated gas temperature profile (left y-axis) and CO production rate (right y-axis) over a straight line in the center of the MW reactor with and without a 5 mm nozzle attached, for a flow rate of a) 20 slm and b) 5 slm. The temperature threshold for net thermal CO_2 dissociation above 3000 K and the zone of recombination between 2000 and 3000 K are also highlighted in the figure.

Figure 17 shows the calculated temperature profile and CO production rate over a straight line at a radial distance of 6.5 mm from the center of the reactor, for a flow rate of 20 and 5 slm without nozzle attached. The temperature profiles indicate that due to the increased convective cooling, the temperature in this part of the reactor is clearly lower at 20 slm compared to 5 slm. At 5 slm the temperature reaches up to 2500 K, while at 20 slm, the gas temperature barely exceeds 2100 K. This was also represented in figure 4, where the high temperature zone extends to a somewhat larger radial distance at 5 slm compared to at 20 slm. At 5 slm, the temperature is high enough for some CO_2 dissociation to occur in this region (i.e., radial distance of 6.5 mm), although at a lower rate than in the

center of the reactor, as the threshold temperature of 3000 K for efficient thermal conversion is not reached. After the plasma, CO recombination still occurs, as indicated by the negative CO production rate, although also at a lower rate than in the center. This indicates that also in this part of the reactor, an improvement in conversion would occur if the gas is quenched after the plasma, as the negative peak of the CO production rate is positioned behind where the nozzle would be placed (as indicated in figure 17). At 20 slm, however, the temperature only reaches up to 2100 K, so that very limited thermal CO_2 dissociation occurs, as shown by the very small peak in CO production rate. Furthermore, the gas temperature does not peak high enough above 2000 K to induce significant recombination reactions. Hence, in this part of the reactor at 20 slm, the limiting factor of the CO_2 conversion process is not CO recombination, but rather the short residence time in the hotter regions of the plasma. As a result, this part of the reactor will not display a significant improvement in CO retention due to quenching, making the overall effect of quenching on the MW reactor performance as a whole less impactful for 20 slm. This is in great contrast to the reactor operating at 5 slm, where CO_2 conversion is limited by recombination also beyond the center of the reactor, where most of the gas flows, and quenching could thus impact the conversion in large parts of the gas stream.

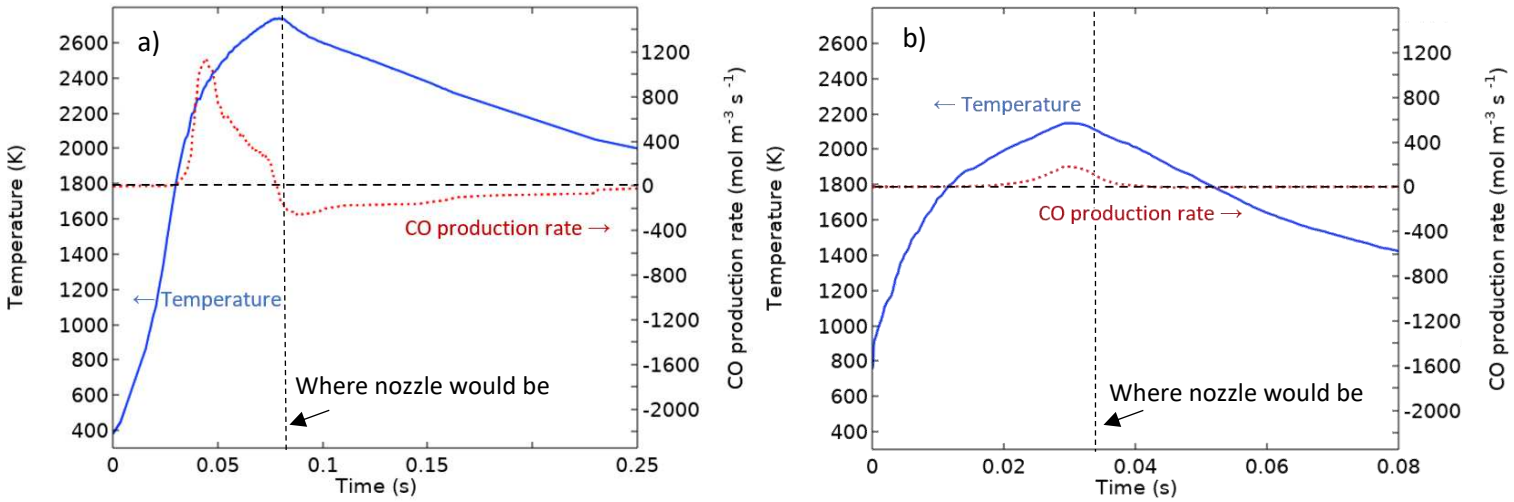

Figure 17: Calculated gas temperature profile (left y-axis) and CO production rate (right y-axis) over a straight line at 6.5 mm from the center of the MW reactor without a nozzle attached, for a flow rate of a) 5 slm and b) 20 slm.

The fact that the CO_2 conversion in the outer layers of the plasma is mainly limited by the residence time at high flow rates (e.g., 20 slm), and mainly by recombination at low flow rates (e.g., 5 slm), is also represented in the experimental results in figure 2. For a reactor without nozzle (black data points), lowering the flow rate from 40 slm down to 10 slm improves the conversion, indicating that conversion could be limited by the residence time, and lowering the flow rate, thus increasing the residence time, the conversion could be enhanced. In general, given the inverse relation between flow rate and SEI, this can be summarized as the SEI being the limiting factor, as at high flow rates the SEI is simply too low to provide enough power to the gas within the short time frame that the gas spends flowing through the active parts of the plasma. Indeed, these data points align with the inverse relation between flow rate and conversion (which is the same as the directly proportional relation between SEI and conversion), indicated by the grey dashed line. Reducing the flow rate to 5 slm, however, does not follow this relation, as the overall conversion drops. Indeed, lowering the flow rate reduces the convective cooling and increases the significance of back reactions in the whole reactor. Figure 2 indicates that below 10 slm, the conversion is mainly limited by recombination, rather than by residence time.

This is further demonstrated in figure 2 when a nozzle is attached to the reactor (blue data points). The greatest improvement is seen at 5 slm, which is most limited by recombination, while smaller improvements are observed at higher flows, when already in the standard case without nozzle there are less recombination reactions. As shown by figure 2, the improvement due to quenching by the 2.5 mm nozzle at 5 slm is so significant, that this case also becomes residence time-limited. Indeed, the recombination reactions are suppressed to the extent that lowering the flow rate from 10 slm to 5 slm enhances the conversion, aligning again with the inverse flow rate-conversion relation.

4. Conclusion

We developed a 3D CFD model and a quasi-1D chemical kinetics model to simulate the effect of quenching nozzles developed by Hecimovic et al., for enhancing the CO_2 conversion in a MW plasma reactor by quenching the recombination reactions in the effluent. Our models show that due to the tangential gas injection, two distinct regions are formed in the reactor: (i) hot gas that swirls in the center of the reactor and (ii) cool gas swirling near the walls, which forms a cool periphery gas flow around the hot center. Without nozzle attached, there is very limited heat transfer between these two regions, and the only cooling present is due to convective cooling from the gas stream, which is more significant at higher flow rates. When a nozzle is attached, the cooling drastically increases in two ways: (i) the small nozzle opening forces the hot gas in the center and the cool gas near the walls to mix, while (ii) the nozzle walls (being water-cooled) induce additional conductive cooling. In this way, the effluent gas can be cooled faster, and to lower temperatures. Our quasi-1D chemical kinetics model shows that the nozzle allows to quickly cool below some important temperature thresholds, i.e. the recombination zone between 2000 and 3000 K. The fast cooling capabilities of the nozzle allow the gas to spend less time in the “recombination zone”, thus limiting the amount of CO lost to recombination reactions.

While the fastest cooling in general (i.e., with nozzle as well as without quenching nozzle) is observed at the higher flow rates, due to the more pronounced convective cooling, the largest improvement due to the quenching nozzles is observed at the lowest flow rate of 5 slm. Due to the strong cooling capabilities of the smallest nozzle of 2.5 mm, we have shown that recombination reactions are suppressed to such an extent that also the low flow rate regime of 5 slm becomes limited by residence time, rather than by recombination, and due to the great reduction of recombination reactions, the conversion enhances by even a factor seven, i.e., from 5% without nozzle, to 35% with quenching nozzle.

5. Acknowledgments

This research was supported by the Excellence of Science FWO-FNRS project (FWO grant ID GoF9618n, EOS ID 30505023), the European Research Council (ERC) under the European Union's Horizon 2020 research and innovation programme (grant agreement No 810182 – SCOPE ERC Synergy project), and through long-term structural funding (Methusalem). The calculations were performed using the Turing HPC infrastructure at the CalcUA core facility of the Universiteit Antwerpen (UAntwerpen), a division of the Flemish Supercomputer Center VSC, funded by the Hercules Foundation, the Flemish Government (department EWI) and the UAntwerpen.

6. References

(1) Hecimovic, A.; D'Isa, F. A.; Carbone, E.; Fantz, U. Enhancement of CO2 Conversion in Microwave Plasmas Using a Nozzle in the Effluent. *J. CO2 Util.* **2022**, *57*, 101870.

(2) IEA. *World Energy Outlook 2021*; Paris, 2021.

(3) IEA. *Net Zero by 2050*; Paris, 2021.

(4) Snoeckx, R.; Bogaerts, A. Plasma Technology-a Novel Solution for CO2 Conversion? *Chem. Soc. Rev.* **2017**, *46*, 5805–5863.

(5) Bogaerts, A.; Kozák, T.; Van Laer, K.; Snoeckx, R. Plasma-Based Conversion of CO2: Current Status and Future Challenges. *Faraday Discuss.* **2015**, *183*, 217–232.

(6) Bogaerts, A.; Neyts, E. C. Plasma Technology: An Emerging Technology for Energy Storage. *ACS Energy Lett.* **2018**, *3*, 1013–1027.

(7) Bogaerts, A.; Centi, G. Plasma Technology for CO2 Conversion: A Personal Perspective on Prospects and Gaps. *Front. Energy Res.* **2020**, *8*, 1–23.

(8) Qin, Y.; Niu, G.; Wang, X.; Luo, D.; Duan, Y. Status of CO 2 Conversion Using Microwave Plasma. *J. CO2 Util.* **2018**, *28*, 283–291.

(9) Wolf, A. .; Peeters, F. J. J.; Groen, P. W.; Bongers, W. A.; van de Sanden, M. C. M. CO2 Conversion in Nonuniform Discharges: Disentangling Dissociation and Recombination Mechanisms. *J. Phys. Chem. C* **2020**, *124*, 16806–16819.

(10) D'Isa, F. A.; Carbone, E. A. D.; Hecimovic, A.; Fantz, U. Performance Analysis of a 2.45 GHz Microwave Plasma Torch for CO2decomposition in Gas Swirl Configuration. *Plasma Sources Sci. Technol.* **2020**, *29*, 105009.

(11) Silva, T.; Britun, N.; Godfroid, T.; Snyders, R. Optical Characterization of a Microwave Pulsed Discharge Used for Dissociation of CO2. *Plasma Sources Sci. Technol.* **2014**, *23*, 025009.

(12) Wolf, A. .; Righart, T. W.; Peeters, F. J.; Bongers, W. .; van de Sanden, M. C. Implications of Thermo-Chemical Instability on the Contracted Modes in CO2 Microwave Plasmas. *Plasma Sources Sci. Technol.* **2020**, *29*, 025005.

(13) van den Bekerom, D. C. M.; Palomares Linares, J. M.; Verreycken, T.; van Veldhuizen, E. M.; Nijdam, S.; Bongers, W.; Van de Sanden, R.; Van Rooij, G. J. The Importance of Thermal Dissociation in CO2 Microwave Discharges Investigated by Power Pulsing and Rotational Raman Scattering. *Plasma Sources Sci. Technol.* **2019**, *28*, 055015.

(14) Vermeiren, V.; Bogaerts, A. Plasma-Based CO2 Conversion: To Quench or Not to Quench? *J.*

Phys. Chem. C **2020**, *124*, 18401–18415.

(15) Viegas, P.; Vialetto, L.; Wolf, A. J.; Peeters, F. J. J.; Groen, P. W. C.; Righart, T. W. H.; Bongers, W. A.; van de Sanden, M. C. M.; Diomede, P. Insight into Contraction Dynamics of Microwave Plasmas for CO2 Conversion from Plasma Chemistry Modelling. *Plasma Sources Sci. Technol.* **2020**, *29*, 105014.

(16) COMSOL Multiphysics® v. 6.0, COMSOL AB: Stockholm, Sweden.

(17) Jones, W. P.; Launder, B. E. The Prediction of Laminarization with a Two-Equation Model of Turbulence. *Int. J. Heat Mass Transf.* **1972**, *15*, 301–314.

(18) Weigand, B.; Ferguson, J. R.; Crawford, M. E. An Extended Kays and Crawford Turbulent Prandtl Number Model. *Int. J. Heat Mass Transf.* **1997**, *40*, 4191–4196.

(19) Magin, T.; Degrez, G.; Sokolova, I. Thermodynamic and Transport Properties of Martian Atmosphere for Space Entry Application. *33rd Plasmadynamics Lasers Conf.* **2002**, No. May.

(20) Van Den Bekerom, D. C. M.; Linares, J. M. P.; Verreycken, T.; Van Veldhuizen, E. M.; Nijdam, S.; Berden, G.; Bongers, W. A.; Van De Sanden, M. C. M.; Van Rooij, G. J. The Importance of Thermal Dissociation in CO2 Microwave Discharges Investigated by Power Pulsing and Rotational Raman Scattering. *Plasma Sources Sci. Technol.* **2019**, *28*, 055015.

(21) Smith, G. P.; Golden, D. M.; Frenklach, M.; Moriarty, N. W.; Eiteneer, B.; Goldenberg, M.; Bowman, T. C.; Hanson, R. K.; Song, S.; Gardiner, W. C. J.; et al. GRI-MECH 3.0.

(22) McBride, B. J.; Zehe, M. J.; Gordon, S. *NASA Glenn Coefficients for Calculating Thermodynamic Properties of Individual Species: National Aeronautics and Space Administration*; 2002.

(23) Carbone, E.; D'Isa, F.; Hecimovic, A.; Fantz, U. Analysis of the C2 (D3Πg-A3Πu) Swan Bands as a Thermometric Probe in CO2 Microwave Plasmas. *plasma sources sci. Technol.* **2020**, *29*, 055003.

(24) Fridman, A. *Plasma Chemistry*; Cambridge University Press: Cambridge, U.K., 2008.

Supporting information

Modelling post-plasma quenching nozzles for improving the performance of CO_2 microwave plasmas

Senne Van Alphen[1,2], Ante Hecimovic[3], Christian K. Kiefer[3], Ursel Fantz[3], Rony Snyders[2], Annemie Bogaerts[1]

[1] Research group PLASMANT, University of Antwerp, Belgium

[2]Research group ChIPS,University of Mons, Belgium

[3] Max-Planck-Institut für Plasmaphysik, Germany

S.1 The finite element mesh

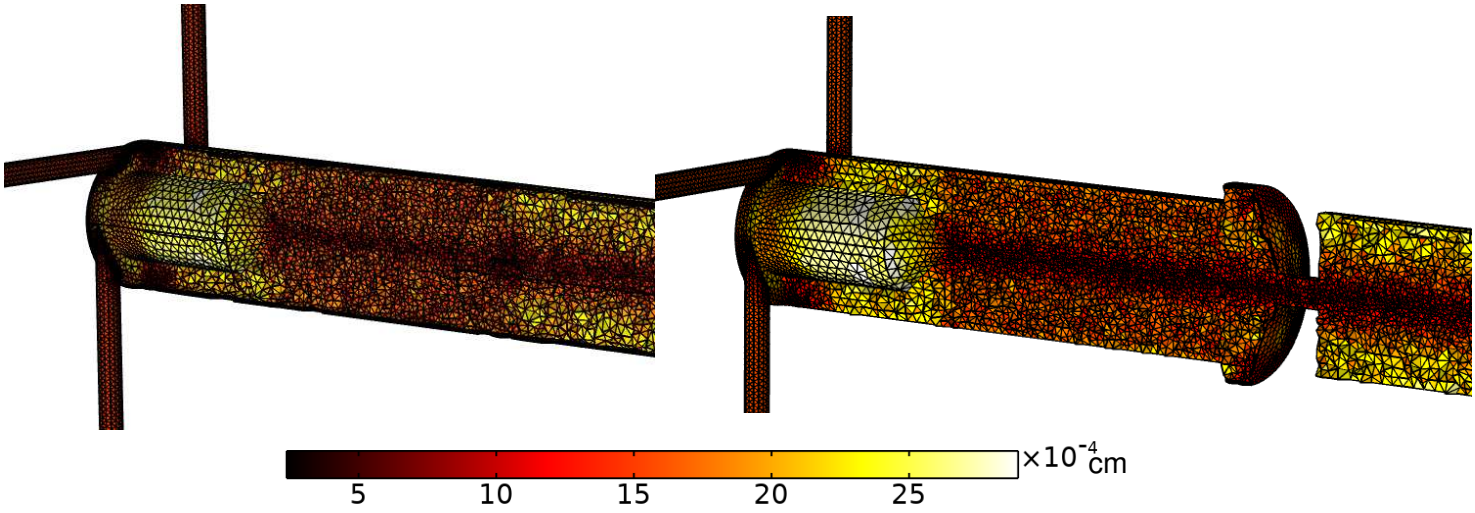

Figure S1: Finite element mesh of the simulation domain of the MW reactor geometry a) without nozzle attached and b) with nozzle attached. The color scale indicates the size of the mesh elements.

Figure S1 presents the finite element mesh of the 3D CFD model domain, in which the color scale indicates the size of the mesh elements. The simulation domain consists of 700 000 tetrahedral-shaped mesh elements, in which the size of the elements is reduced specifically in zones where physical properties are expected to display high gradients, e.g. in the center of the reactor where the plasma filament is located, in the throat of the nozzle, in the inlet tubes. To resolve the thin boundary layers of the fluid along the no-slip boundaries (i.e. u = 0 m/s) of the reactor walls , the finite element mesh near the walls consists of 4 mesh boundary layers with dense element distribution in the normal direction along the walls of the reactors.

This mesh was refined by re-solving the model on progressively finer meshes until the solution remained mesh independent. In this form, the models take 6-10h to solve (without parallelization) on a desktop equipped with an Intel Core i7-5820K CPU and 64.0 GB RAM, using a relative tolerance of 0.001 as conversion criterium.

S.2 The turbulent gas flow

We apply the Menter's Shear Stress Transport (SST) model,[1] which uses the common k-ε model in the free stream and combines it with the more accurate k-ω model near the walls, where the flow is more complicated.

This approach includes the following equations for the turbulent kinetic energy k and the specific dissipation ω:

$$\rho_g(\overrightarrow{u_g}.\nabla)k = \nabla\cdot[(\mu+\mu_T\sigma_k)\nabla k] + P - \beta_0\rho_g\omega k \qquad (S.1)$$

$$\rho_g(\overrightarrow{u_g}.\nabla)\omega = \nabla\cdot[(\mu+\mu_T\sigma_\omega)\nabla\omega] + \frac{\gamma}{\mu_T}\rho_g P - \beta_0\rho_g\omega^2 + 2(1-f_{v1})\frac{\sigma_{\omega2}\rho_g}{\omega}\nabla k\cdot\nabla\omega \qquad (S.2)$$

Where ρ_g stands for the gas density, $\overrightarrow{u_g}$ is the gas flow velocity vector, μ is the dynamic viscosity, σ_k, σ_ω and γ are model coefficients defined in equations S.10, S.11 and S.12 below, and β_0 and $\sigma_{\omega2}$ are dimensionless model constants defined in table S1. The other symbols are explained below.

In equations S.1 and S.2, μ_T is the turbulent viscosity of the fluid and is defined as:

$$\mu_T = \frac{a_1 k}{max(a_1\omega, Sf_{v2})} \qquad (S.3)$$

In which S is the absolute strain rate and a_1 is a dimensionless model constant, defined in table S1. In equations S.2 and S.3, f_{v1} and f_{v2} are two blending functions that control the switch from the k-ω model to the k-ε model in the free stream (where f_{v1} = 1)

$$f_{v1} = \tanh\left(\min\left(\theta_2^2, \frac{4\sigma_{\omega2}k}{CD_{k\omega}y^2}\right)\right)^4 \qquad (S.4)$$

$$f_{v2} = \tanh(\theta_2^2) \qquad (S.5)$$

In which y is the y-component of the position vector, and θ_2 and $CD_{k\omega}$ are placeholders for the following terms:

$$CD_{k\omega} = max\left(2\rho\sigma_{\omega2}\frac{1}{\omega}\frac{\partial k}{\partial x}\frac{\partial\omega}{\partial x},\ 10^{-10}\right) \qquad (S.6)$$

$$\theta_2 = max\left(\frac{2\sqrt{k}}{\beta_0\omega l_W^2}, \frac{500\mu}{y^2\omega}\right) \qquad (S.7)$$

In which l_W is the wall distance.

In equations S.1 and S.2, P serves as a product limiter coefficient and is defined as:

$$P = \min(P_k 10\rho\beta_0 k\omega) \quad (S.8)$$

In which P_k is a placeholder for the following term:

$$P_k = \mu_T \left(\nabla\overrightarrow{u_g} \cdot \left(\nabla\overrightarrow{u_g} + \left(\nabla\overrightarrow{u_g}\right)^T\right) - \frac{2}{3} \cdot \left(\nabla \cdot \overrightarrow{u_g}\right)^2\right) - \frac{2}{3}\rho k \nabla \cdot \overrightarrow{u_g} \quad (S.9)$$

The model coefficients in equations S.1 and S.2 are defined as:

$$\sigma_k = f_{v1} \cdot \sigma_{k1} + (1 - f_{v1})\sigma_{k2} \quad (S.10)$$

$$\sigma_\omega = f_{v1} \cdot \sigma_{\omega 1} + (1 - f_{v1})\sigma_{\omega 2} \quad (S.11)$$

$$\gamma = f_{v1} \cdot \gamma_1 + (1 - f_{v1})\gamma_2 \quad (S.12)$$

In which σ_{k1}, σ_{k2}, $\sigma_{\omega 1}$,$\sigma_{\omega 2}$, γ_1 and γ_2 are dimensionless model constants, defined in table S1.

Table S1: Dimensionless model constants used in the SST turbulent flow model.

σ_{k1}	0.85
σ_{k2}	1
$\sigma_{\omega 1}$	0.5
$\sigma_{\omega 2}$	0.856
γ_1	0.5556
γ_2	0.44
a_1	0.31
β_0	0.09

S.3 Gas flow velocity profiles of the quasi-1D chemical kinetics model

Using the axial gas flow velocity calculated by the 3D CFD model, we can convert the time dependence of a 0D chemical kinetics model to a spatial dependence over a straight line in the reactor, resulting in a quasi-1D model. The axial gas flow velocity profiles in the center of the reactor, which are used in this conversion, are presented for two different flow rates in figure S2, for a) a reactor without and b) a reactor with 5 mm nozzle attached. The figures clearly display the increase in gas flow velocity as the gas flows through the narrow nozzle gap.

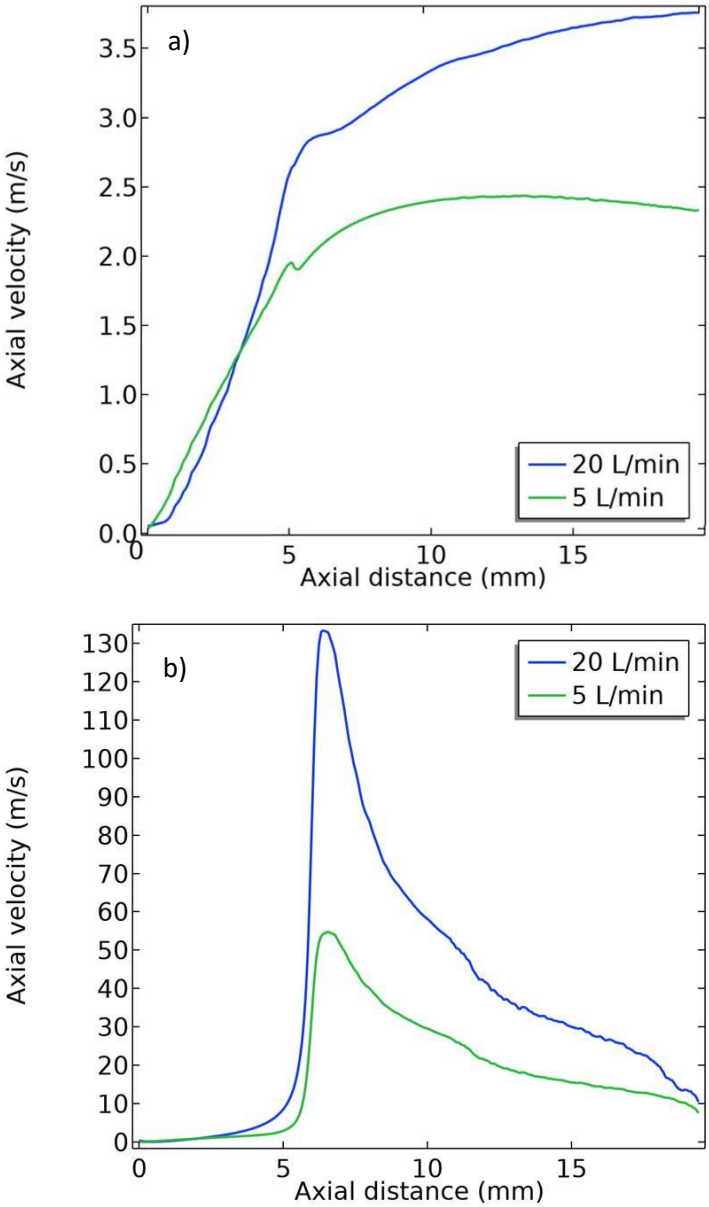

Figure S2: Axial velocity profile in the center of the reactor as calculated by the 3D CFD model for a reactor a) without and b) with 5 mm nozzle attached.

S.4 Boundary conditions in the model

For the calculation of the gas flow velocity field $\vec{u}$ (u,v,w) and pressure p inside the reactor, the following boundary conditions are introduced in the model geometry when solving the Navier-Stokes equations (equations 1 and 2 of the main paper):

At the Inlet:

$$\vec{u} = \vec{u}_0 \tag{S.13}$$

In which $\vec{u}_0$ is the flow velocity defined by the input flow rate.

$$k = \frac{3}{2}(u_0 I_T)^2 \tag{S.14}$$

$$\omega = \frac{k^{\frac{1}{2}}}{(\beta_0)^{\frac{1}{4}} L_T} \tag{S.15}$$

Where u_0 is the input flow rate, I_T the expected turbulence intensity (here 0.05 for medium intensity), β_0 a dimensionless model constants shown in table S1 and L_T the turbulence length scale.

At the reactor walls:

$$\vec{u} = 0 \tag{S.16}$$

Where the velocity is zero as a result of the "no slip" condition at the walls.

At the outlet:

$$\left[-p\vec{I} + \mu(\nabla\vec{u} + \nabla(\vec{u})^T) - \frac{2}{3}\mu(\nabla \cdot \vec{u})\vec{I}\right]\vec{n} = p_0\vec{n}_{outlet} \tag{S.17}$$

In which p_0 is the pressure at the outlet, and $\vec{n}_{outlet}$ the unit vector normal to the outlet boundary.

For the calculation of the gas temperature T_g, the following boundary conditions are introduced in the model geometry when solving the heat balance equation (equation 3 of the main paper):

At the Inlet:

$$-\vec{n}_{inlet} \cdot \vec{q} = \rho\vec{u}\int_{T_{inlet}}^{T} C_p dT_g \cdot \vec{n}_{inlet} \tag{S.18}$$

In which T_{inlet} is the gas temperature of the inlet stream, usually 293.15 K, and $\vec{n}_{inlet}$ the unit vector normal to the inlet boundary.

At the reactor walls:

For the heat loss through the reactor walls to the environment at a heat loss rate q_{loss}, the boundary condition states:

$$-\vec{n}_{wall} \cdot \vec{q} = q_{loss} \tag{S.19}$$

$$q_{loss} = h(T_{ext} - T_g) \qquad (S.20)$$

In which $\vec{n}_{wall}$ is the unit vector normal to the wall boundary, T_{ext} is the gas temperature of the environment, usually 293.15 K and h the heat transfer coefficient of the reactor wall material (10 W/(m²*K) for the quartz tube).

At the outlet:

$$-\vec{n}_{outlet} \cdot \vec{q} = 0 \qquad (S.21)$$

In which $\vec{n}_{outlet}$ is the unit vector normal to the wall boundary.

S.5 The thermodynamic and transport properties of the model

All thermodynamic and transport properties of the gas, i.e. the viscosity, the thermal conductivity and the heat capacity are adopted from Magin et al.[2], where these properties are calculated for a wide range of temperatures assuming thermodynamic equilibrium. This means that changes in gas composition and energy balance due to chemical reactions are taken into account within these properties, e.g. the endothermic characteristic of CO_2 splitting, as well as the formation of CO and O_2 and the destruction of CO_2 are represented in the heat capacity and thermal conductivity. However, as these properties are calculated assuming thermodynamic equilibrium, the properties assume that chemical equilibrium is reached very fast as the temperature increases or decreases. This assumption is reasonable in an atmospheric MW plasma torch, because at 6000 K, which is the core temperature of the plasma filament, chemical equilibrium is reached within milliseconds, which is very fast compared to the timescale of the residence time in the reactor (in the seconds range). In the effluent of the reactor, however, chemical equilibrium is reached slower, so the impact of chemistry on the heat balance is not completely accounted for in this part of the reactor. However, at this point the heat balance is mostly defined by the hot gas flowing form the 6000 K plasma zone, rather than recombination reactions heating the gas, which makes the error of the assumption relatively small.

S.6 Representing the plasma as a heat source

By representing the plasma as a heat source using the thermal balance equation (equation 3 in the main paper), the 3D shape of the plasma is required as input for the model.

This heat source term (Q) is then defined as:

$$Q = N * rad(x) * rad(y) * ax(z)$$

In which rad and ax are the radial and axial power profiles of the MW power, respectively, and N is a normalization factor, such that:

$$\iiint Q\, dx\, dy\, dz = P_{MW}$$

Where P_{MW} is the microwave power that is absorbed by the plasma, measured in the experiments. The radial and axial power profiles (rad and ax) are defined using analytical functions that approximate the radial and axial profile of a contracted plasma filament, as measured by D'Isa et al.[3] and Wolf et al.[4]. The radial power profile used in the model, is shown in figure S3a, resembling closely the profile measured by D'Isa et al., shown in figure S3b. The axial power profile used in the model, is shown in figure S4a, resembling closely the profile measured by D'Isa et al., shown in figure S4b. Furthermore, as concluded in the work from D'Isa et al., the plasma diameter and length of the plasma is independent on the flow,[3] allowing us to use the same power profile for every flow rate.

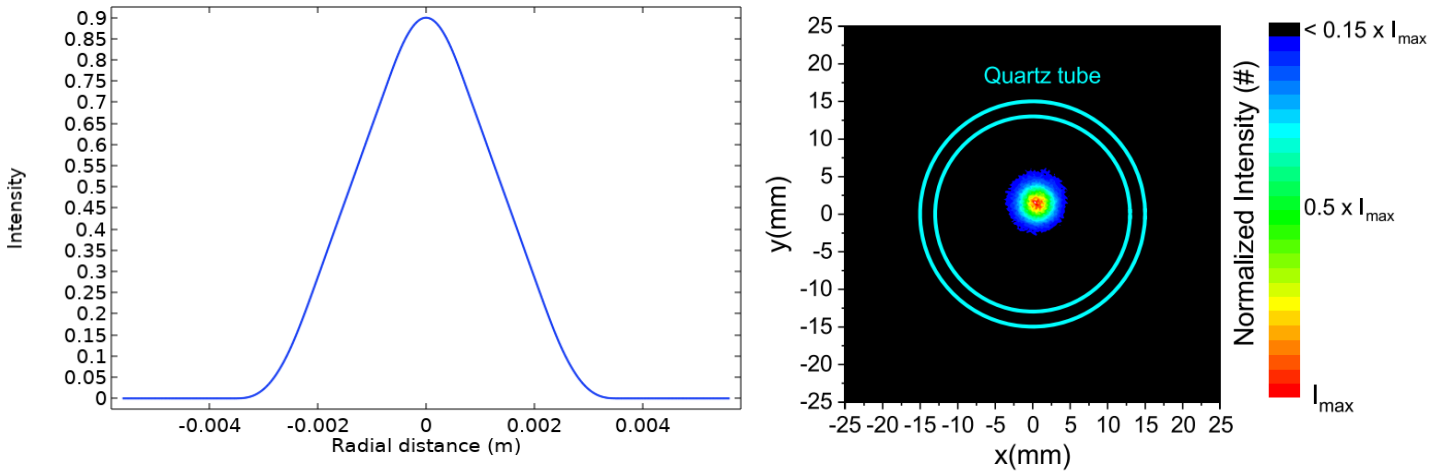

Figure S3: a) Radial power density profile of the plasma assumed in the model b) Radial ICCD image taken by D'Isa et al

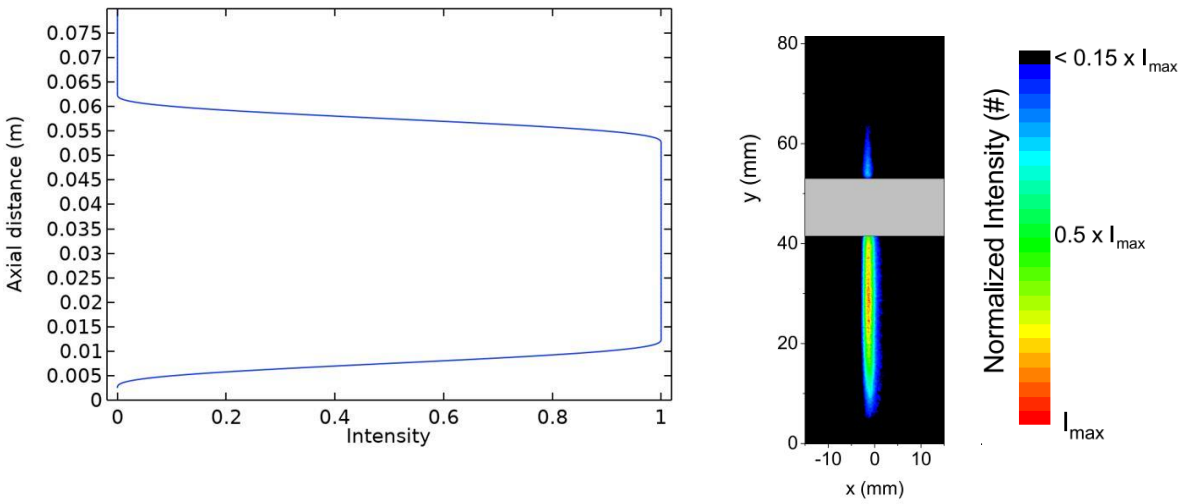

Figure S4: a) Axial power density profile of the plasma assumed in the model b) Axial ICCD image taken by D'Isa et al.

References

(1) Menter, F. R.; Kuntz, M.; Langtry, R. Ten Years of Industrial Experience with the SST Turbulence Model Turbulence Heat and Mass Transfer. *Turbul. Heat Mass Transf.* **2003**, *4*, 625–632.

(2) Magin, T.; Degrez, G.; Sokolova, I. Thermodynamic and Transport Properties of Martian Atmosphere for Space Entry Application. *33rd Plasmadynamics Lasers Conf.* **2002**, No. May.

(3) D'Isa, F. A.; Carbone, E. A. D.; Hecimovic, A.; Fantz, U. Performance Analysis of a 2.45 GHz Microwave Plasma Torch for CO2. *Plasma Sources Sci. Technol.* **2020**, *29*.

(4) Wolf, A. .; Righart, T. W.; Peeters, F. J.; Bongers, W. .; van de Sanden, M. C. Implications of Thermo-Chemical Instability on the Contracted Modes in CO2 Microwave Plasmas. *Plasma Sources Sci. Technol.* **2020**, *29*, 025005.